Journal of Materials Chemistry A

PAPER

View Article Online
View Journal | View Issue

Cite this: J. Mater. Chem. A, 2019, 7, 1055

Newly designed 1,2,3-triazole functionalized covalent triazine frameworks with exceptionally high uptake capacity for both CO_2 and H_2†

Soumya Mukherjee,[ab] Monojit Das,[ab] Anupam Manna,[ab] Rajamani Krishna [c] and Sanjib Das *[ab]

The search for efficient and high performing physisorbents for CO_2 capture and separation from point sources as well as storage of cleaner gaseous fuels, such as H_2 and/or CH_4, is considered to be a major challenge of numerous ongoing research activities in the domain of functional porous materials to avoid global warming *via* stabilizing the atmospheric CO_2 level. Herein, a set of novel 1,2,3-triazole functionalized covalent triazine frameworks (TzCTFs) was synthesized under typical ionothermal conditions utilizing two rationally designed C3-symmetric triazole-substituted aromatic trinitrile building block analogues, namely Tz-FCN and Tz-HCN, with fluorinated and non-fluorinated phenyl core, respectively. A comparative and comprehensive elucidation to the effect of building block functionalities on the textural and gas uptake properties of resulting TzCTFs has been discussed. TzCTF materials synthesized at 600 °C give rise to significantly higher BET surface area (*df*-TzCTF600: 1720 m^2 g^{-1} and TzCTF600: 1582 m^2 g^{-1}) compared to the TzCTF400 (874 m^2 g^{-1}) and *df*-TzCTF400 (906 m^2 g^{-1}) material synthesized at 400 °C. The dominating ultra-micropores in the range of 0.45–0.9 Å, together with embedded various CO_2-phillic basic trizolic, triazine, and pyrrolic N-species, were synergistically endowed with an exceptionally high uptake of both CO_2 (up to 6.79 mmol g^{-1} at 273 K) and H_2 (up to 2.50 wt% at 77 K) under the pressure of 1 bar. Notably, the *df*-TzCTF600 with CO_2 uptakes of 4.60 mmol g^{-1} (298 K, 1 bar) and 6.79 mmol g^{-1} (273 K, 1 bar), along with H_2 uptake capability of 2.50 wt% (77 K, 1 bar), ranks highest among all related CTF-based adsorbents under identical conditions to date. The methane uptake capacity of *df*-TzCTF600 (4.37 wt% at 273 K, 1 bar) is also impressive and represents the second highest among all porous organic polymers. Moreover, TzCTFs exhibit moderately high CO_2 selectivity over N_2 with a CO_2/N_2 selectivity of up to 27 (Henry) and 40 (IAST) at 298 K. Finally, the obtained novel TzCTF materials in combination with facile modular synthesis *via* rationally designed building blocks, high thermal and chemical stability, and excellent CO_2, H_2 and CH_4 uptake and separation capabilities make them promising task-specific adsorbents for various potential applications.

Received 23rd August 2018
Accepted 4th December 2018

DOI: 10.1039/c8ta08185a

rsc.li/materials-a

Introduction

With rapid growth of global population and industrialization, the atmospheric concentration of carbon dioxide has increased radically because of increasing consumption of fossil fuels, which is widely accepted as one of the major contributors to global warming.[1] According to the International Energy Agency (IEA), development of appropriate cost-effective highly efficient materials for carbon dioxide capture and separation from point source post-combustion effluents, like flue gas and storage of cleaner gaseous energy sources such as hydrogen and methane, has a phenomenal potential to reduce CO_2 emission to a significant extent and, ultimately, slow down the climate change.[2,3] Currently, amine scrubbing is the only adopted CCS technology for industrial CO_2 capture and separation *via* an energy-intensive chemisorption process (enthalpy of adsorption, $\sim Q$ > 40 kJ mol^{-1}).[4] However, it suffers from severe drawbacks, including corrosion of the equipment, energy penalty regeneration, and environmentally unfriendly expensive disposal process of the amine solution upon its expiration.[4,5] In order to achieve cost-effective and environmentally-benign CO_2 capture, an extensive search of efficient novel

[a]Department of Colloids & Materials Chemistry, CSIR-Institute of Minerals & Materials Technology, Bhubaneswar 751013, Odisha, India. E-mail: sanjibdas@immt.res.in

[b]Academy of Scientific & Innovative Research (AcSIR), Ghaziabad 201002, India

[c]Van't Hoff Institute for Molecular Sciences, University of Amsterdam, Science Park 904, 1098 XH Amsterdam, The Netherlands

† Electronic supplementary information (ESI) available: Synthesis of building blocks and their characterization *via* FT-IR and NMR spectroscopy, powder XRD, CHN, gas (N_2 and CH_4) uptakes of TzCTFs, selectivity calculation using Henry's law method and ideal adsorption solution theory, detailed information about column breakthrough simulation for CO_2/N_2 mixture under kinetic flow condition. See DOI: 10.1039/c8ta08185a

porous organic polymers (POPs)[6–16] has emerged. These polymers are a promising potential alternative to the current technology owing to their fast adsorption kinetics, governed by a highly reversible physisorption *via* weak van der Waals forces (enthalpy of adsorption $\sim Q$ < 40 kJ mol^{-1}).[17] On the other hand, the decreasing number of sources of fossil fuel, and climate change, caused by anthropogenic carbon dioxide emission, have spurred a tremendous effort to store clean, high energy density gaseous fuels, particularly H_2, as an alternative energy source for the replacement of current carbon-based energy sources *via* advancement of hydrogen and fuel cell power technologies in transportation, stationary, and portable application in order to meet the global environmental and energy demands.[18]

During the last decade, covalent triazine frameworks (CTFs), a subclass of porous organic polymers (POPs), have drawn enormous attention as emerging materials for a variety of applications, including gas adsorption and separation,[19–28] catalysis,[29–32] water purification,[33,34] energy storage,[35,36] and sensing.[37] Unlike traditional solid adsorbents, such as zeolites (*e.g.* zeolite 13X and 5A),[38,39] metal–organic frameworks,[40–42] activated carbons,[43–46] and chemically functionalized mesoporous materials,[47–49] CTF-based adsorbents exhibit high tolerance for moisture along with a large accessible surface area, tailored pore size, low skeleton density, superior thermal and chemical stability, and functional and structural diversity resulting in a plethora of polymerization reactions and judicious limitless choice of organic building blocks. Since the development of CTF by Kuhn *et al.* in 2008,[50] various approaches have been adopted, such as alteration of reaction temperature, changing molar ratio of monomer to $ZnCl_2$, utilization of multidentate building blocks, mixed ligands and carbonization of as-synthesized CTFs to prepare a variety of CTFs as high-performance CO_2 adsorbents.[51–54] However, the most intensively investigated approach is the covalent introduction of polar hetero-atoms, particularly nitrogen, oxygen, and fluorine functionalities, onto the pore surfaces of CTFs, utilizing hetero-atom functionalized nitrile building blocks that enable enhanced dipole–quadrupole interactions between the pore surface and CO_2 gas molecules.[55–58] Although significant efforts have been made in the area of CTF materials modification, only limited dimensionality, framework functionality, polymerization, and topology alteration of these important classes of materials have been addressed. There is no "ideal" building block and/or polymerization condition for the synthesis of highly efficient CTFs. Thus, introduction of different building blocks comprising various functionalities and investigation of new or modified polymerization conditions are still highly desired to better realize the effect of chemical functionalization on the targeted framework structures, controlling the textural properties and functional efficiencies for targeted applications. Recent theoretical studies show that multi-N-containing heteroaromatic ring systems, such as guanidine, 7-azaindole, melamine, 1,2,3-triazole, and 1,2,4-triazole, are ideal for designing new porous materials for high capacity storage and separation of CO_2 gas, because they interact more strongly with CO_2 compared to the well known functional systems, such as amine and fluorine.[59]

Therefore, motivated by recent theoretical investigation of the role of multi-N-containing hetero-aromatic rings in CO_2 capture as well as versatile tunable and modular chemistry of CTFs, herein we report for the first time the synthesis of a novel series of triazole functionalized CTF-based materials (abbreviated onwards as TzCTFs), derived from two newly designed C3-symmetric 1,2,3-trizole substituted aromatic trinitrile building blocks, namely Tz-FCN and Tz-HCN, as a high-capacity storage platform for both CO_2 and H_2 (Scheme 1). Our strategy of selecting Tz-FCN and Tz-HCN monomers is manifold: (i) conventional $ZnCl_2$ mediated typical cyclotrimerization of nitrile functional groups of Tz-HCN and Tz-FCN would lead to porous CTFs, where CO_2 adsorption would be facilitated through dipole–quadrupole interactions between the triazine N atom and CO_2 gas molecule inside the frameworks, (ii) introduction of a thermally labile C–F bond into the Tz-FCN building block would result in additional ultra-microporosity (<0.7 nm) in the resulting CTF materials *via* well documented defluorination and the subsequent etching phenomenon during high temperature ionothermal process,[60] which would further enhance CO_2 and H_2 adsorption capability as ultra-micropores are most desirable trapping small gas molecules like CO_2 and H_2, and (iii) incorporation of highly polar multi-N-containing 1,2,3-triazole heteroaromatic units into porous networks would significantly impact promoting CO_2 uptake capacity, owing to highly favorable and stronger electrostatic interactions between triazole units and CO_2 gas molecules. As described below, the above-desired properties are all found in our four triazole functionalized CTF-based materials, namely *df*-TzCTF600, *df*-TzCTF400, TzCTF600, and TzCTF400, synthesized *via* $ZnCl_2$ mediated ionothermal process operated at 400 °C and 600 °C (Scheme 1). Current study describes the synthesis and comprehensive characterization of four TzCTFs derived from Tz-FCN and Tz-HCN building blocks, followed by their small gas, particularly CO_2, CH_4, and H_2, uptake capabilities and selective CO_2 binding over CH_4 and N_2. Furthermore, the present study also demonstrates the CO_2 capture and separation under kinetic flowing mixed gas (CO_2/N_2) condition, using column breakthrough simulation, relevant to industrial post-combustion capture. With the concept of present building block design, the current work would give insight into the preparation of new series of efficient solid adsorbents with

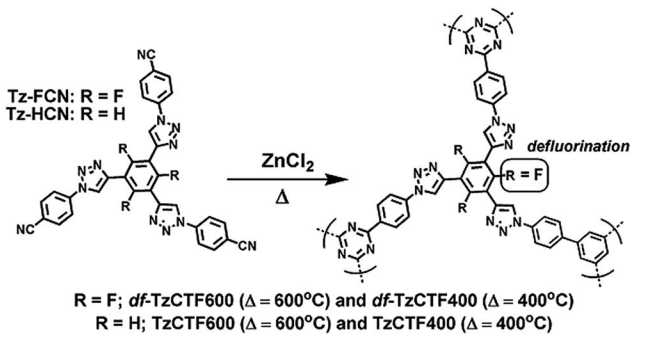

Scheme 1 Schematic representation of the synthetic route of proposed TzCTFs.

tunable porous architectures, which would have potential applications over a wide range of technological interests.

Experimental

General procedure for the preparation of TzCTFs

Syntheses of TzCTFs were carried out in ionothermal conditions as reported by Kuhn *et al.*[50] with some modifications as follows. In a typical experimental procedure, aromatic trinitrile building block (0.5 g) and anhydrous $ZnCl_2$ (10 equivalents) salt were transferred into a quartz ampoule (1.8 × 12 cm) under an inert atmosphere. The ampoule was then evacuated, sealed under vacuum, and then heated at the defined temperature for 48 hours. After the ampoule was cooled down to room temperature and opened (**Caution**: ampoule is under high pressure which is released while opening), the black solid was collected and stirred in distilled water (200 ml) for 48 hours to remove most of the $ZnCl_2$ salt. The product was isolated by filtration and further stirred in 1 N HCl (200 ml) for 48 hours to further remove the residual salt. The resulting black solid was filtered and washed successively with water, alcohol, and acetone and finally dried under vacuum at 100 °C for 6 hours.

Results and discussion

To incorporate triazole moiety into the CTF network, we have designed and synthesized two new nitrogen-rich C3-symmetric triazole substituted aromatic trinitrile building blocks, namely Tz-FCN and Tz-HCN, *via* versatile copper(I)-catalyzed click reaction[61] between the respective alkyne and 4-azido benzonitrile, as depicted in Scheme S1.† Both building blocks are formed as solid precipitates, which are insoluble in all common organic solvents. The Tz-FCN and Tz-HCN building blocks, having large π-conjugated aromatic structures, were characterized through powder X-ray diffraction (PXRD), solid-state ^{13}C cross polarization-magic angle spinning (CP-MAS) nuclear magnetic resonance, Fourier transformation infrared (FT-IR) spectroscopy, and elemental analysis because of their complete insolubility in common organic solvents (Fig. S1–S3†). TzCTFs were synthesized *via* ionothermal reactions between nitrile building block, Tz-HCN and Tz-FCN, in molten $ZnCl_2$ inside a sealed quartz tube, where $ZnCl_2$ is acting both as a Lewis acid catalyst and a solvent. As reported earlier, the ratio of $ZnCl_2$/building block, polymerization temperature and duration are crucial for structural and functional properties of CTF-based materials.[50,54,56,62] In general, higher ratios of $ZnCl_2$/building block, such as 5 : 1 to 10 : 1, as well as higher reaction temperature, 400 to 600 °C, are the most desirable synthetic parameters to introduce enhanced textural and functional properties *via* different extent of structural degradation in such materials.[23,51,56,60,63,77,94] Moreover, high $ZnCl_2$/building ratio takes care of the solubility issue of monomers having comparatively higher mass during ionothermal reaction, which is essential for occurrence of polymerization process in a uniform and controlled manner. Therefore, a molar ratio of $ZnCl_2$ to nitrile of 10 : 1 was chosen, keeping view of high molecular weight of our Tz-HCN and Tz-FCN monomers. Both polymerization reactions were performed at 400 and 600 °C temperatures. With the above specified reaction conditions, polymerization reactions were performed for 48 hours leading to a black monolithic material in a moderate yield in each case. These materials were completely insoluble in any common organic solvent, including diluted aqueous solution of HCl and NaOH, implying their excellent framework stability and chemical inertness. The successful synthesis of fully condensed TzCTFs was first confirmed by FT-IR (Fig. 1a). The characteristic intense band at around 2230 cm^{-1}, attributed to C≡N stretching modes, disappears completely demonstrating total conversion of monomers *via* trimerization reaction has taken place. Meanwhile, two weak and extremely broad IR bands in the range of 1300–1360 cm^{-1} and 1560–1580 cm^{-1} appeared in all TzCTFs, corresponding to the characteristic C–N stretch and the quadrant stretch of the triazine rings, although the bands are not clearly visible (highlighted green).[20,57,60]

But, an additional characteristic breathing mode of the triazine units is clearly visible at around 790 cm^{-1} (highlighted green) in the spectra of TzCTF materials synthesized at 400 °C, while this band almost disappears in the spectra of materials synthesized at 600 °C.[24,64] Moreover, a strong broad band at around 1609 cm^{-1} (highlighted violet) was easily identified in all TzCTFs, attributing to the characteristic –N=N– stretching frequency originating from 1,2,3-triazole ring, confirming the presence of triazole unit in TzCTFs.[65–67] Therefore, FTIR analysis proves ongoing carbonization of all TzCTFs during the ionothermal reaction and subsequent decomposition of both triazine and triazole moieties, which become more prominent with increasing synthesis temperature from 400 °C to 600 °C.

Solid-state ^{13}C NMR spectroscopy is used to gather additional, more detailed local structural information of newly synthesized TzCTFs, as shown in Fig. 2. All TzCTFs show a broad NMR signal spanning from 170 to 100 ppm for 400 °C materials, TzCTF400 and *df*-TzCTF400, while for 600 °C materials such as TzCTF600 and *df*-TzCTF600, the signal is located in the range of 170 to 90 ppm. The signal constituting aromatic region is strong for 400 °C materials, whereas it becomes much weaker and broader for TzCTF600 and *df*-TzCTF600, indicating higher degree of carbonization with increasing synthesis temperature. The presence of a 1,2,3-triazole moiety is indicative by the resonance of two triazolyl carbons[67,68] at around 135–148 ppm and 160–175 ppm for the triazine carbons[56,69] of triazine unit, depending upon the local electronic structures of these heterocyclic rings. In our TzCTF materials, triazine resonance peak appeared at ~162 ppm. The relative intensity of triazine resonance peak is very small for TzCTF400 and *df*-TzCTF400 because of high intensity of aromatic signals, whereas it becomes very visible as a distinct peak for TzCTF600 and *df*-TzCTF600 as the aromatic resonance peaks are weak. But, obvious proof for the existence of triazine units is still elusive in all TzCTFs. However, the existence of triazol moiety is confirmed by the presence of a shoulder peak at around 146 ppm with reasonable intensity corresponding to the resonance of triazolyl carbons. By considering both FT-IR and solid-state NMR results, we conclude that carbonization and decomposition of both triazole and triazine units have

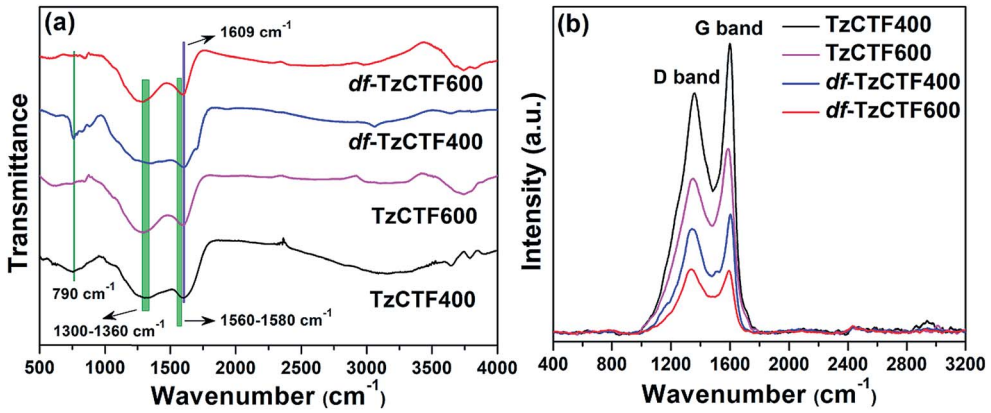

Fig. 1 (a) FT-IR and (b) Raman spectra of TzCTFs.

occurred. These processes are more pronounced with the high synthesis temperature materials, TzCTF600 and *df*-TzCTF600.

The fine structure of TzCTFs was elucidated by wide-angle powder X-ray diffraction (Fig. S4†) and Raman spectroscopy (Fig. 1b). The XRD profiles of TzCTFs not showing any sharp peaks indicate the formation of disordered and largely amorphous structures, which is most common in CTFs family except for a few examples of CTF materials, such as CTF-0, CTF-1, and CTF-2 that show moderate crystallinity.[50,70,71] However, all TzCTFs exhibit a weak, extremely broad diffraction peak centered at around 23.66° 2θ for TzCTF400 and TzCTF600, whereas for *df*-TzCTF400 and *df*-TzCTF600, it is located at around 24.91° 2θ. The peaks at 2θ = 23.66° and 24.91° correspond to the 002 reflections where d_{002} values are about 3.75 and 3.57 Å, respectively, which are larger than the characteristic d_{002} value of 3.35 Å observed for pure graphitic layer frameworks.[72] Thus, XRD analysis of TzCTFs indicates the existence of low degree graphitic wall structures where nitrogen containing graphene layers are arranged in a turbostratic fashion *via* weak interlayer coupling. Raman spectroscopy is an effective analytical technique for deep understanding of the structure and identifying the doping effect of heteroatom doped carbon materials.[73] In Raman spectra of TzCTFs, the intense sharp Raman shift in the region of 2200–2250 cm^{-1}, characteristic for the aromatic nitrile group, disappears completely, indicating the completeness of polymerization process, which is consistent with the results obtained from FT-IR analysis. As shown in Fig. 1b, all TzCTFs exhibit virtually superimposed, two well-defined broad Raman bands peaking at around 1360 cm^{-1} and 1600 cm^{-1}, assigned to the D band and G band, respectively. The origin of the D band is attributed to the presence of disordered carbon structures, while the G band is associated with the first-order scattering of the E_{2g} mode of sp^2 hybridized carbon atoms in a two-dimensional hexagonal graphitic layer structure.[74,75] These two Raman active peaks resemble those, typically appearing in graphitized carbon materials, further indicating partial graphitization of all TzCTF materials.[76] The I_D/I_G peak ratios of TzCTF400, TzCTF600, *df*-TzCTF400, and *df*-

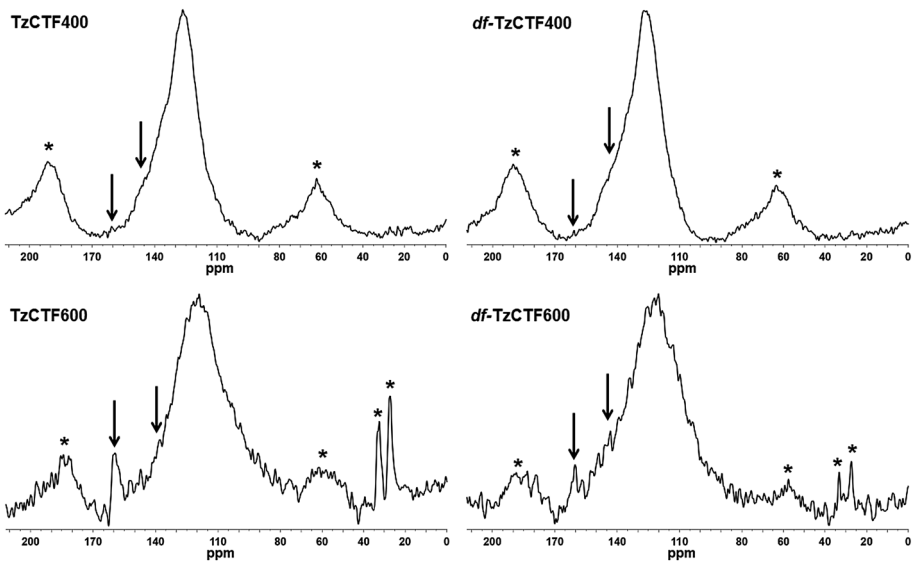

Fig. 2 ^{13}C CP/MAS solid-state NMR spectra of TzCTFs. Spinning side bands are starred.

TzCTF600 were estimated to be 0.83, 0.88, 0.89, and 1.02, respectively, and ascend with increasing polymerization temperature. Moreover, *df*-TzCTF400 and *df*-TzCTF600 present slightly higher I_D/I_G ratio compared to that of TzCTF400 and TzCTF600 materials, thus, indicating that TzCTFs synthesized from fluorinated building block possess more structural defects than the TzCTFs materials, prepared from a non-fluorinated building block analog. Based on the powder X-ray diffraction and Raman spectra analysis, TzCTFs are considered to be partially graphitic in nature, comprising both small graphitic layers and disordered amorphous carbon. To get further insight into their chemical composition, the extent of degradation, and bonding patterns of TzCTFs, elemental analysis (EA) and high resolution X-ray photoelectron spectroscopy (XPS) measurements were performed. Combustion elemental analysis reveals a significantly higher C/N ratio than the theoretically calculated values and it slowly grows with the increase in temperature (Table S1†). This attributes to the fact that a partial decomposition of TzCTFs took place during the polymerization process, and it presumably occurs mainly *via* C–H and [CN]-elimination, as observed in many previously reported CTF-based materials, predominantly in those prepared by using higher molar ratio ($\geq$10) of monomer to $ZnCl_2$ salt.[77,78] The XPS survey spectra of TzCTFs (Fig. 3) consist of only carbon, nitrogen, and oxygen spectroscopic signatures. There were no residual peaks associated with inorganic impurities, particularly zinc species such as $ZnCl_2$ used in excess as major components during the polymerization reaction, which was further confirmed by ICP-OES analysis. The complete removal of inorganic impurities during acid-water washing process indicates the existence of well-organized, interconnected porous structures of TzCTFs. Furthermore, the survey scans (Fig. S5†) revealed the absence of fluorine in both *df*-TzCTF400 and *df*-TzCTF600, synthesized at 400 °C and 600 °C, respectively. The complete defluorination phenomenon associated with the *df*-TzCTF400 and *df*-TzCTF600 materials is in good agreement with previously reported data on CTFs materials, synthesized using higher amount (10 equivalent) of $ZnCl_2$, where it is evident that trimerization of nitrile and subsequent defluorination carbonization takes place during the polymerization process.[55,60] Moreover, the complete defluorination process leads to *in situ* generation of highly reactive species, CFn, which are responsible for etching the polymeric backbone while coming out from the polymeric matrix.[55,60] This defluorination process is the major cause of structural defects in *df*-TzCTF materials synthesized from fluorinated building blocks, compared to the TzCTF materials derived from non-fluorinated building block analogs, which well verifies the result obtained from Raman analysis. The existence of oxygen, plausibly due to partial oxidation of TzCTFs during polymerization, atmospheric oxygen, and/or moisture trapped within the frameworks, is in accordance with the literature reports.[60,79] To assess the chemical bonding nature of C and N atoms in the TzCTFs, the high resolution core-level XPS spectra for C 1s and N 1s are measured, as depicted in Fig. 3. The C 1s spectra of TzCTFs can be deconvoluted into four peaks with binding energies of 284.6, 285.56–285.63, 286.50–286.52, and 290.04–290.07 eV. The dominant peak centered at 284.6 eV is ascribed to the sp^2-hybridized graphitic carbon atoms (C=C), whereas the peak with binding energy ranging 285.53–285.59 eV is usually attributed to the sp^3-hybridized carbon atom bonded to nitrogen/oxygen atom (C–O and/or C–N). The peak with binding energy ranging 286.50–286.52 eV is assigned as the sp^2-hybridized carbon atom attached to electronegative oxygen/nitrogen atom (C=N and/or C=O), while the weakest deconvoluted peak with binding energy ranging 290.04–290.07 is associated as π–π^* transitions.[65,80,81] The existence of the intense peak of sp^2-C atoms together with a very weak peak of π–π^* transitions clearly suggest the partially graphitic layer structures of TzCTF materials, which is consistent with results obtained from powder XRD and Raman spectra analysis.

Similarly, the N 1s spectra of TzCTFs can be deconvoluted into four peaks with binding energies of 398.6, 400.29–400.33, 401.30–401.33, and 402.55–402.57 eV. The first peak, centered at 398.6 eV, corresponds to hexagonal pyridinic nitrogen (–C=N–) that mainly comes from the triazine rings of TzCTFs. The second peak, located in the range of 400.29–400.33 eV, is attributed to pyrrolic nitrogen species, while the third peak, ranging 401.30–401.33 eV, is identified as doubly bonded nitrogen atom (–N=N–), originating from the triazole units in the framework.[80,82,83] The weakest fourth peak ranging 402.55–402.57 eV is due to oxidized N–O species.[83] The modalities of TzCTFs were further characterized by field-emission scanning electron microscopy (FE-SEM) and high resolution transmission electron microscopy (HRTEM). The FE-SEM images of TzCTFs display a typical morphology of agglomerated tiny particles with almost regular shapes and homogenously distributed sizes (Fig. 4). As shown in Fig. 4, TzCTFs networks are composed of well-distributed uniform porous frameworks, as revealed by HRTEM analysis. Bright contrast strips under the focused image represent the interconnected hexagonal layer structure, while dark contrast cores display empty channels and pores. Thermogravimetric analysis shows that all four materials exhibit exceptionally high thermal stability with minimum weight loss even at 500 °C. The small amount of mass loss below 100 °C is attributed to the removal of remaining hydrated water inside the TzCTFs networks.

To investigate the porosity parameters of TzCTFs (Table 1), N_2 adsorption–desorption experiments were carried out at 77 K. All samples were degassed at 140 °C for 12 h under vacuum prior to the gas sorption measurement. According to the IUPAC classification, all TzCTFs exhibit a combination of type-I & II adsorption isotherm (Fig. 5). The sharp increase of nitrogen uptake in the low relative pressure ($p/p_0 < 0.01$) indicates the existence of abundant micropores and ultra-micropores in the frameworks.[84] A small degree of apparent hysteresis between adsorption and desorption isotherms was observed, which is attributed to the presence of an additional low degree of mesoporosity in all TzCTFs.[84] The graphs of *df*-TzCTF600 and TzCTF600 show hysteresis spanning the relative low pressure range of 0.4–0.9, indicating the presence of well developed additional mesopores, while the hysteresis spans almost the entire range of p/p_0 = 0–0.9 for *df*-TzCTF400 and TzCTF400, resembling a slight H4-type, which is typically observed for materials with narrow slit-shaped pores and strong gas binding

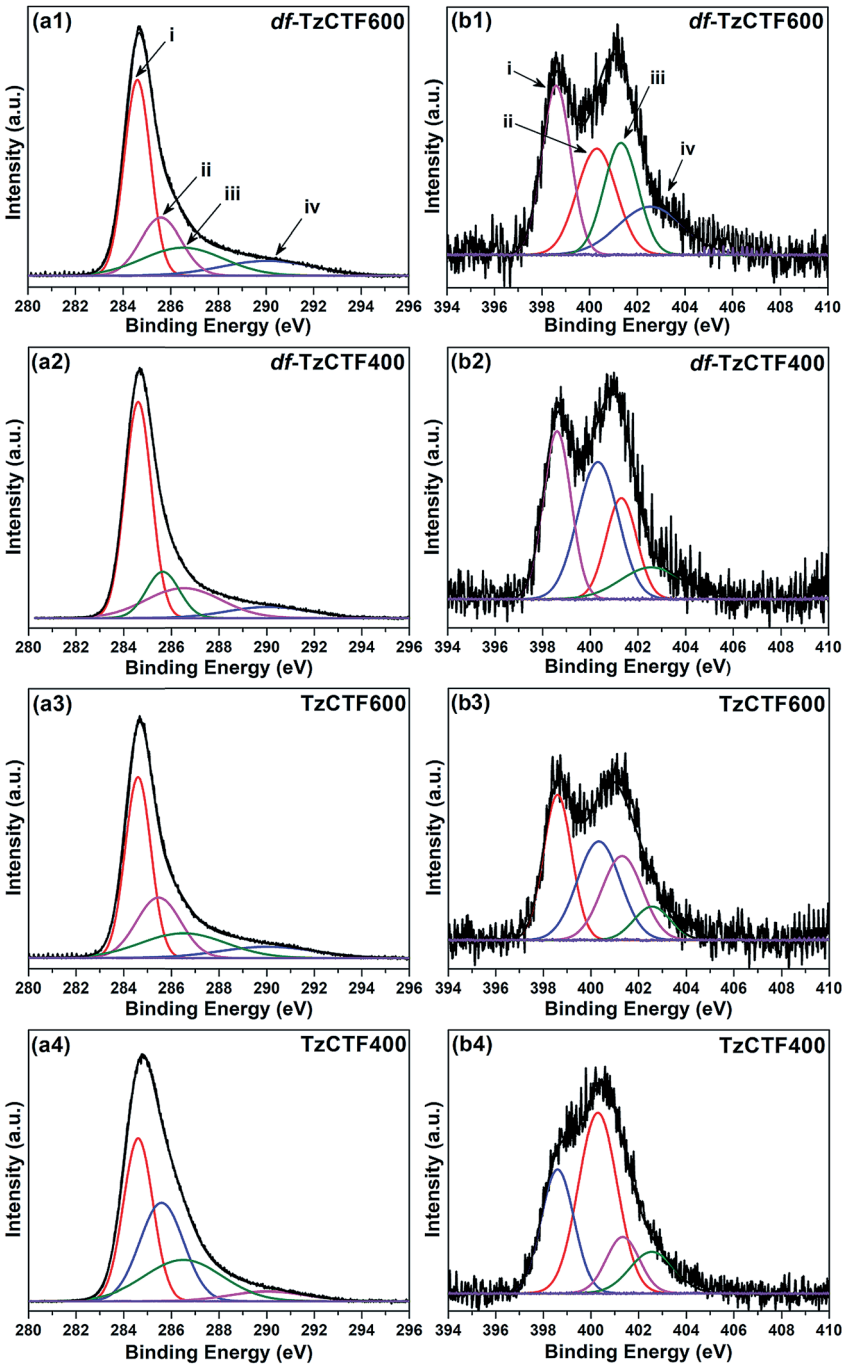

Fig. 3 XPS spectra of TzCTFs materials: (a1–a4) C 1s [i: C=C; ii: C–O, C–N; iii: C=O, C=N; iv: π–π* transition] and (b1–b4) N 1s [i: triazine C=N; ii: pyrrolic N species; iii: trizolic N=N; iv: oxidized N–O species].

on the pore surface.[85] The calculated Brunauer–Emmett–Teller (BET) specific surface areas[86] over the pressure range p/p_0 = 0.05–0.3 were found to be in the following order: *df*-TzCTF600 (1720 $m^2 g^{-1}$) > TzCTF600 (1582 $m^2 g^{-1}$) > *df*-TzCTF400 (906 $m^2 g^{-1}$) > TzCTF400 (874 $m^2 g^{-1}$) and the Langmuir surface areas for TzCTFs series are 2238 $m^2 g^{-1}$, 1127 $m^2 g^{-1}$, 1926 $m^2 g^{-1}$, and 1110 $m^2 g^{-1}$, for *df*-TzCTF600, *df*-TzCTF400, TzCTF600, and TzCTF400, respectively. The obtained surface areas are comparable with other previously reported high performing CTF and POP-based materials in the literature (see ESI†). The total pore volumes estimated at $p/p_0 = 0.99$ are 1.12 $cm^3 g^{-1}$ (*df*-TzCTF600), 1.02 $cm^3 g^{-1}$ (TzCTF600), 0.70 $cm^3 g^{-1}$ (*df*-TzCTF400), and 0.69 $cm^3 g^{-1}$ (TzCTF400). This trend indicated that BET surface area and total pore volume of TzCTFs increase significantly when polymerization is carried out at 600 °C compared to that at 400 °C. However, upon further increase of synthesis temperature to 700 °C, the resulted *df*-TzCTF700 and

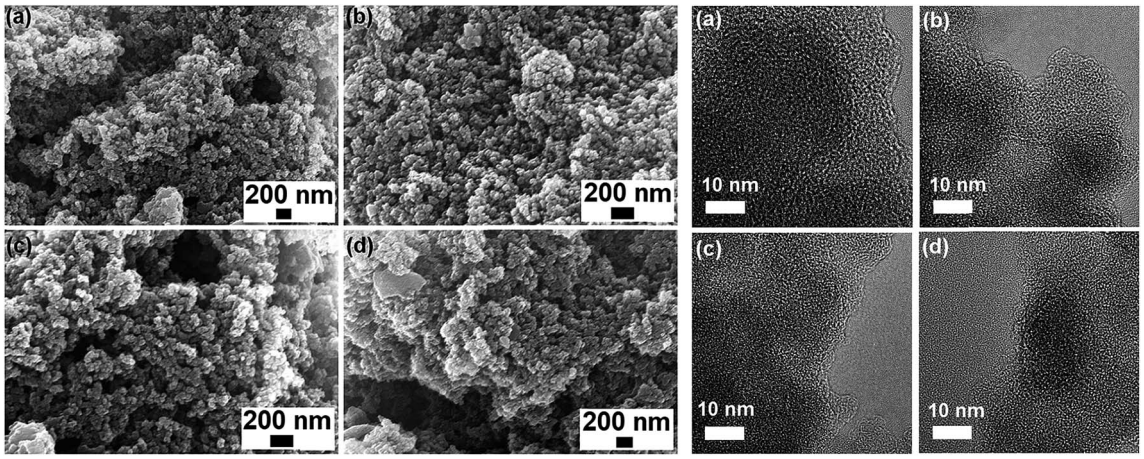

Fig. 4 FE-SEM images (left) and HRTEM images (right): (a) *df*-TzCTF600, (b) *df*-TzCTF400, (c) TzCTF600, and (d) TzCTF400.

TzCTF700 materials display inferior textural properties compared to their respective 600 °C materials (see ESI†).

Pore size distribution (PSD) is the crucial parameter characterizing porous materials. N_2 isotherms ($T = 77$ K) based PSD of TzCTF materials were calculated by non-local density functional theory (NL-DFT) using "carbon-based slit-pore" model (Fig. 6a).

All TzCTFs mainly comprise a significant fraction of micropores with pore diameters smaller than 2 nm and a very small fraction of broad pore-size distribution over 2 nm, corresponding to the presence of additional mesopores. The degree of microporosity can be evaluated from N_2 adsorption isotherms by calculating the ratio of microporous volume to total pore volume ($V_{0.1}/V_{tot}$).[87] The TzCTF series showed $V_{0.1}/V_{tot}$ values ranging from 0.51 to 0.67, indicating the abundance and dominance of micropores in these materials. Moreover, the PSD of TzCTFs, based on N_2 adsorption isotherms measured at 77 K, suggest the presence of significant amount of ultra-micropores (<0.7 nm). However, the diffusion rate of N_2 molecules with micropores filling particular pores, smaller than 0.7 nm at extremely low relative pressure ($<10^{-5}$), is quite slow at 77 K, which might lead to under-equilibration of measured N_2 adsorption isotherms giving inaccurate results.[88,89] Associated with low diffusion rate of N_2 molecules at 77 K, ultramicropores filling requires extremely low relative pressure measurement ($\geq 10^{-7}$) that leads to time-consuming measurements.

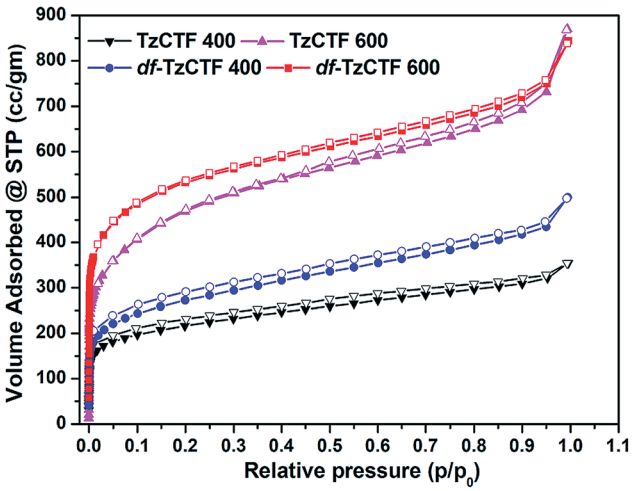

Fig. 5 Nitrogen adsorption–desorption isotherms of TzCTFs measured at 77 K (solid and open symbols represent adsorption and desorption, respectively).

Moreover, argon adsorption at 87 K also has limitations since pore filling of ultramicropores still occurs at a very low relative pressure and restricted diffusion of argon molecules at such cryogenic temperature (87 K). This prevents argon molecules from entering the narrowest ultramicropores (<5 Å) despite the

Table 1 Porosity data derived from N_2 isotherm (77 K, 1 bar) of TzCTFs materials

Compound	S_{BET}[a] ($m^2\ g^{-1}$)	S_{Lang}[b] ($m^2\ g^{-1}$)	$V_{0.1}$[c] ($cm^3\ g^{-1}$)	V_{tot}[d] ($cm^3\ g^{-1}$)	$V_{0.1}/V_{tot}$	V_{micro}[e] (CO_2) ($cm^3\ g^{-1}$)
df-TzCTF400	906	1127	0.40	0.70	0.57	0.081
df-TzCTF600	1720	2238	0.75	1.12	0.67	0.084
TzCTF400	874	1110	0.35	0.69	0.51	0.052
TzCTF600	1582	1926	0.64	1.02	0.62	0.056

[a] Calculated BET surface area over the pressure range 0.05–0.3 P/P_0. [b] Langmuir surface area calculated by applying Langmuir equation to nitrogen adsorption isotherm over the pressure range 0–0.15 P/P_0. [c] Micropore volume calculated at $P/P_0 = 0.1$ for pores with diameter smaller than 1.6 nm. [d] Total pore volume calculated at $P/P_0 = 0.99$. [e] Total pore volume for pores with diameters smaller than 0.9 nm at $P/P_0 = 0.1$ calculated from CO_2 adsorption isotherm at 273 K (NL-DFT model).

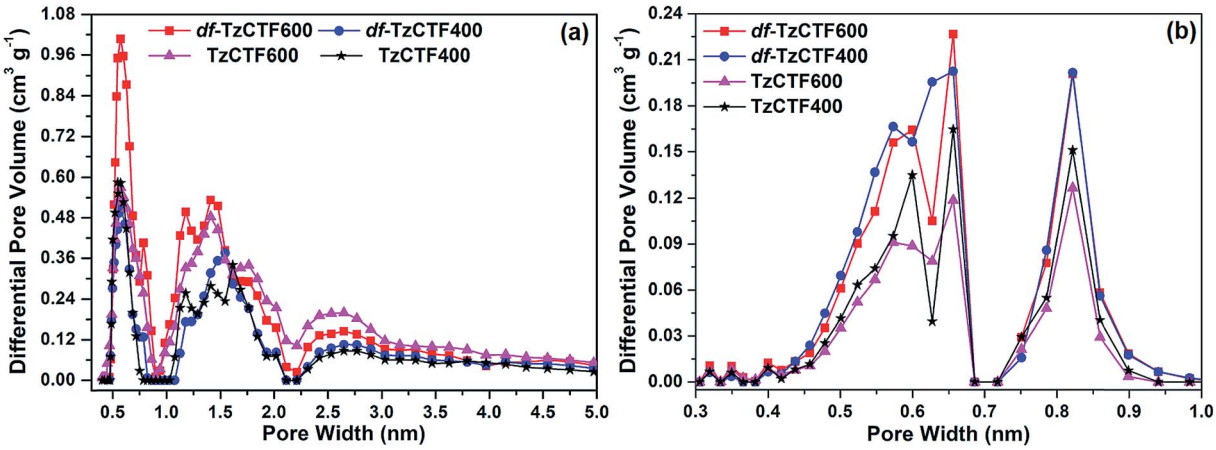

Fig. 6 Pore size distribution curve of TzCTFs derived from (a) N_2 adsorption isotherm (at 77 K) and (b) CO_2 adsorption isotherm (at 273 K) using NL-DFT method.

fact that argon is non-interacting in nature with a variety of pore surface functional groups.[56,90] Therefore, to achieve faster equilibrated adsorption and extended range of narrowest ultramicropores analysis with a greater degree of accuracy, CO_2 adsorption analysis at 273 K can be performed.[91–93] The saturation pressure of CO_2 at 273 K is 26 141 Torr; it ensures faster and equilibrated adsorption analysis in the range of moderate absolute pressure (1–760 Torr) with higher accuracy.

In addition, high saturation pressure of CO_2 at 273 K with large diffusion rate and smaller kinetic diameter (0.33 nm) allows more easy access to CO_2 molecules entering into the ultramicropores (down to ~0.35 nm) compared with nitrogen (kinetic diameter 0.36 nm) and argon (kinetic diameter 0.34 nm) molecules at cryogenic temperature. Therefore, CO_2 adsorption isotherm at 273 K was used to derive better resolved PSD in the ultramicroporous region spanning 0.3 to 1.0 nm by non-local density functional theory (NL-DFT), using "carbon-based slit-pore" model. The TzCTFs display similar kind of PSD patterns of pores down to 1.0 nm (Fig. 6b). However, a careful examination of PSD curves shows that the dominance of significant fractions of micro- and ultra-micropores in *df*-TzCTF600 and *df*-TzCTF400 is greater compared to that of TzCTF600 and TzCTF400 materials. One of the most obvious reasons for the occurrence of higher ultra-micropores is the elimination of F-functional groups as reactive species like CF_4, C_2F_4, and F_2 from the resulting polymer networks during high temperature polymerization process.[55] This observation is in accordance with previous literature reports on the thermal decomposition of fluorine-functionalized materials.[60] The release of fluorinated decomposition products etches the polymeric networks, thereby, creating additional narrow micropores. Therefore, this is in good agreement with our hypothesis that incorporation of F atoms by replacing H atoms in the phenyl core of Tz-HCN building blocks would lead to a higher degree of ultra-micropores (<7 Å) in the resulting polymer networks (*df*-TzCTF600 and *df*-TzCTF400). This is one of the major decisive factors achieving enhanced gas uptake and separation properties for any kind of microporous materials.

The co-existence of abundant narrow- and ultra-micropores along with remarkably high thermal and chemical stability of the current set of TzCTF materials motivated us to explore their potential for uptake of cleaner energy source gases, particularly H_2 and CH_4. The H_2 adsorption isotherm measurements were carried out at $T = 77$ K and 1 bar (Fig. 7b). Table 2 summarizes the H_2 uptake from all the scrutinized TzCTF materials. The *df*-TzCTF600 exhibits the highest H_2 uptake of 2.50 wt% followed by *df*-TzCTF400, TzCTF600, and TzCTF400 with uptake capacities of 2.16, 2.06, and 1.75 wt% respectively. Noteworthy, the H_2 uptake capability of *df*-TzCTF600 (2.50 wt%) measured at ambient pressure supersede all reported CTF based materials under identical conditions, as summarized in Table S7.† Methane is the primary component of natural gas and a potential bridging fuel to a low-carbon energy future.[94] Fig. 7a shows that *df*-TzCTFs exhibits extremely high methane uptake near ambient temperature and pressure condition. The *df*-TzCTF600 and *df*-TzCTF400 with CH_4 uptake capacity of 4.37 wt% (2.72 mmol g^{-1}) and 3.58 wt% (2.23 mmol g^{-1}), respectively, that are significantly higher than many highly efficient POP-based CH_4 adsorbets at 273 K and 1 bar. But, with the only exception of recently reported TPC-1 (6.2 wt%, 273 K and 1 bar) material. Comparison table of current scenario of low pressure CH_4 uptake adsorbents based on porous organic polymers is given in Table S6.† It is worth mentioning here that both hydrogen and methane uptake capacity are reduced down upon further increasing the synthesis temperature to 700 °C (see ESI†).

The search for structure–property relationship for CO_2 uptake revealed that suitable pore size commensurate with the kinetic diameter of a CO_2 molecule and strong interactions between the porous frameworks and CO_2 molecules are the most decisive features for enhancing the CO_2 uptake and separation capacity. All TzCTFs comprises relatively small pore sizes dominated in the range 0.45–0.9 Å, which is most favorable for CO_2 uptake and thereby, separation of CO_2 from other relatively larger kinetic diameter gases like CH_4 and N_2. In addition, the presence of CO_2-phillic multi-N-containing

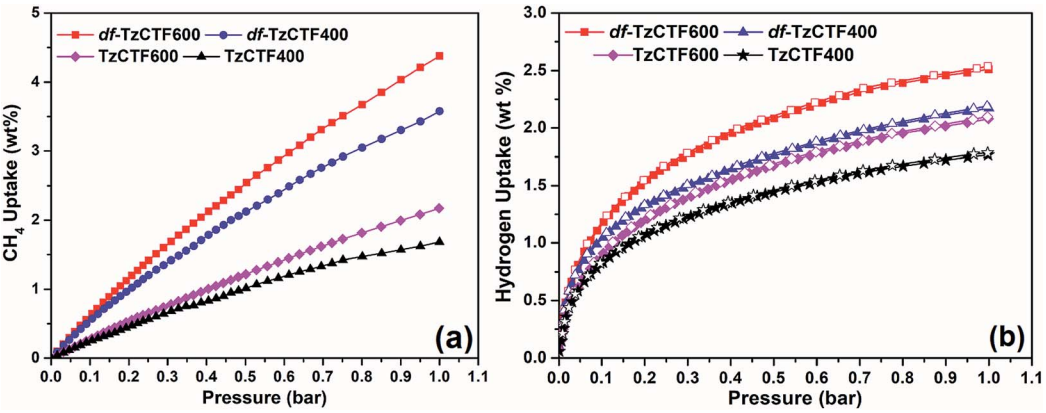

Fig. 7 (a) CH_4 adsorption of TzCTFs measured at 273 K, (b) H_2 adsorption (solid symbols) and desorption (open symbols) isotherms for TzCTFs measured at 77 K.

triazole and triazine units including pyrrolic N species inside TzCTFs scaffolds is another desirable feature, which can be expected to further enhance the CO_2 uptake capability of TzCTFs frameworks. Therefore, the CO_2 uptake efficiency of all TzCTFs was assessed by CO_2 isotherms recorded at $T = 273$ K, 298 K, and 308 K (Fig. 8) up to 1 bar, which is summarized in Table 2. As shown in Fig. 8, TzCTFs show remarkably high CO_2 uptake capacities, both at low (0.15 bar) and ambient pressure (1.0 bar), which are significantly higher for defluorinated TzCTF materials than those of their counterparts synthesized from non-fluorinated building block analog. The CO_2 uptake capacity (6.79 mmol g^{-1}) of *df*-TzCTF600 at $T = 273$ K under ambient pressure is exceptionally high and outperforms the CO_2 uptake capabilities of recently reported best performing CTF-based adsorbents, such as FCTF-1-600 (5.53 mmol g^{-1}),[55] *bipy*-CTF600 (5.58 mmol g^{-1}),[56] CTF-py (5.08 mmol g^{-1}),[95] HAT-CTFs-450/600 (6.30 mmol g^{-1})[23] and imine-linked 3D porous organic framework PPF-1 (6.07 mmol g^{-1}).[96] Therefore, to the best of our knowledge, *df*-TzCTF600 with CO_2 uptake capacities of 6.79 mmol g^{-1} ($T = 273$ K, 1 bar) possesses the highest adsorption values reported for any CTF-based adsorbents so far. The *df*-TzCTF400, synthesized at the lower temperature (400 °C), also shows impressive CO_2 uptake capability with 5.51 mmol g^{-1} at $T = 273$ K at ambient pressure, which is comparable to other high performing CO_2 adsorbents reported in the literature, as depicted in Table S7.† Similarly, *df*-TzCTF600 with 4.60 mmol g^{-1} of CO_2 uptake capability at 298 K and ambient pressure ranks highest among the claimed so far best performing CO_2 adsorbents, such as FCTF-1-600 (3.41 mmol g^{-1}),[55] CTF-py (3.79 mmol g^{-1}),[95] *bipy*-CTF600 (3.07 mmol g^{-1})[56] in the CTF family and very recently reported NRPP-2 (3.71 mmol g^{-1})[97] in the POP fraternity at $T = 298$ K and ambient pressure. Comparison of CO_2 capture performances and structural parameters of best performing reported CTF materials, measured under identical conditions, are summarized in Table S7.† However, the CO_2 uptake capacity decreases as the synthesis temperature increases to 700 °C (see ESI†). The decreased gas adsorption capabilities of 700 °C materials compared to those of 600 °C materials are plausibly due to the inferior textural properties, caused by greater degree of carbonization and structural decomposition.

The exceptionally high CO_2 uptake capabilities of TzCTFs further motivated us to explore their potential under conditions closest to those of post-combustion CO_2 capture, where absorbents would inevitably be exposed to moisture.[98] To explore the influence of moisture on CO_2 uptake, degassed samples were stored at open atmospheric conditions (~60% relative humidity condition) for seven days, while CO_2 uptake capacities of humidified samples were remeasured at different time intervals during that period. Fig. 9a shows retention of CO_2 uptake capacity by TzCTFs stored at open atmospheric conditions, where in all cases, above 70% CO_2 uptake capacities were

Table 2 Summary of gas uptake properties for the presented TzCTFs series

	CO_2 uptake[a]				CH_4 uptake[c]		H_2 uptake[c]	Selectivity[d]
Material	273 K	298 K	308 K	Q_{st}[b]	273 K	298 K	77 K	298 K
df-TzCTF400	5.51 (2.02)	3.32	2.32	36	3.58	2.06	2.16	40 (27)
df-TzCTF600	6.79 (2.17)	4.60	3.00	34	4.37	2.19	2.50	30 (21)
TzCTF400	4.21 (1.38)	2.55	1.90	32	1.74	1.16	1.75	26 (24)
TzCTF600	4.40 (1.27)	2.51	2.03	28	2.17	1.25	2.06	21 (17)

[a] Gas uptake in mmol g^{-1} at 1 bar and values in parenthesis in mmol g^{-1} at 0.15 bar. [b] Isosteric heat of adsorption at zero coverage in kJ mol^{-1}. [c] Gas uptake in wt% at 1 bar. [d] Calculated by IAST method at molar ratio of 15/85 for CO_2/N_2 and values in parenthesis are calculated from the ratio of the initial slopes in the Henry region of the respective CO_2 and N_2 adsorption isotherms.

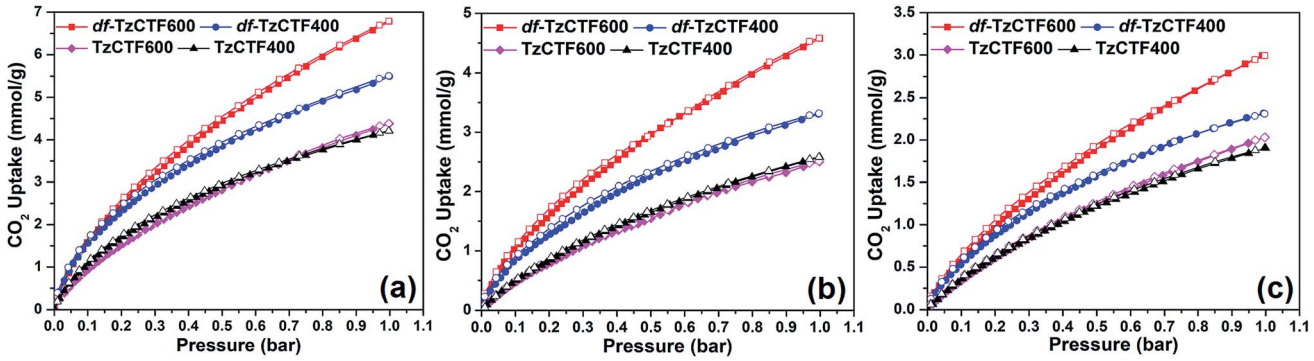

Fig. 8 CO_2 adsorption (filled symbols) and desorption (open symbols) isotherms of TzCTF series measured at (a) 273 K, (b) 298 K, and (c) 308 K.

retained even after 7 days, which is better than that of many reported best performing porous solid CO_2 adsorbents.[99,100] The original CO_2 uptake capacity is restored to its original value after redegassing the samples. Furthermore, we investigated recyclability performance of *df*-TzCTF600 using Autosorb-iQ Quantachrome instrument under both vacuum and temperature swing modes. In recyclability experiments, regeneration cycles were carried out by evacuating the sample under ultra-high pressure for one hour under ambient temperature or heating it at 60 °C at ambient argon atmosphere, followed by CO_2 uptake analysis at $T = 273$ K. After five consecutive regeneration cycles, the *df*-TzCTF600 almost completely retains its original CO_2 uptake capacity (Fig. 9b). For low pressure post-combustion capture, such as flue gas applications where CO_2 content is only ~15% at a total pressure of 1 bar, a large CO_2 uptake capability at 0.15 bar (CO_2 partial pressure in flue gas) is a key feature that better highlights the adsorbent efficiency. As shown in Table 2, all TzCTFs exhibit impressive amount of CO_2 uptake at 0.15 bar, which is comparable or higher than that many best known porous organic polymers like PAN-2 (1.97 mmol g^{-1}),[101] PPN-6-SO_3Li (2.02 mmol g^{-1}),[102] PECNOF-3 (1.43 mmol g^{-1}),[103] CPOP-1 (1.22 mmol g^{-1}),[104] and F-DCBP-1 (2.15 mmol g^{-1}),[57] measured under identical conditions. In fact, the uptake capacity of 2.17 mmol g^{-1} of CO_2 at 273 K and 0.15 bar of *df*-TzCTF600 makes it the best performing adsorbent after the very recently reported HAT-CTFs.[23] The presence of high number of ultramicropores and active CO_2-phillic basic N-species in the form of triazine, triazole, and pyrrolic units is largely responsible for outstanding low pressure CO_2 capability by TzCTFs. From the available CO_2 and N_2 single-gas adsorption isotherms of TzCTFs, adsorption selectivity of CO_2 over N_2 at an equilibrium partial pressure of 0.85 bar (N_2) and 0.15 bar (CO_2) in the bulk phase was evaluated by adopting the ideal adsorption solution theory (IAST) model. As shown in Table 2, all TzCTFs display moderate to good gas selectivity for CO_2/N_2 gas mixtures, derived from IAST model at 298 K and 1 bar with IAST selectivity value of 30, 40, 21 and 26 for *df*-TzCTF600, *df*-TzCTF400, TzCTF600 and TzCTF400, respectively. The IAST selectivity value of our highest performing *df*-TzCTF600 material is comparable or higher than those of many well-known related porous organic polymers, such as FCTF-1-600, F-DCBP-CTF1, CTF-py, and *bipy*-CTF600, reported in the literature (Table S7†).[56,57,95] Recent report shows that to increase selectivity of CO_2 over N_2, introduction of nitrogen phobic functionality, particularly nitrogen rich azo group into the polymeric networks is the most effective pathway.[105] However, azo-functionalized POPs lead to moderate CO_2 uptake capability as azo group has moderate affinity for CO_2, unlike polar triazine and/or triazole based moieties. For the sake of completeness, the CO_2/N_2 selectivity was finally calculated for TzCTFs by utilization of the ratio of initial slopes, estimated from Henry's law constant for single-component CO_2 and N_2 adsorption isotherms, measured at 298 K. The estimated values are listed in Table 2.

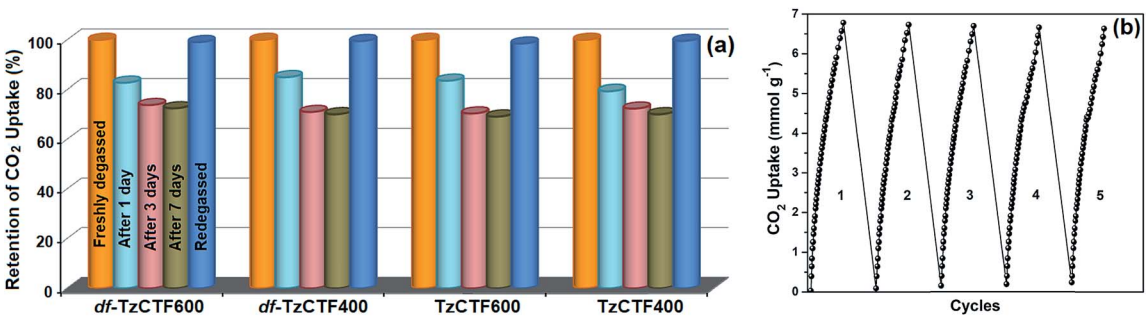

Fig. 9 (a) CO_2 uptake at 298 K and 1 bar with humidified TzCTFs samples. (b) Five cycles of CO_2 uptake at 273 K and 1 bar by the *df*-TzCTF600 sample.

Towards better understanding of the binding affinity between TzCTF networks and CO_2 molecules, the isosteric heat of adsorption (Q_{st}) was calculated with a variant of the Clausius–Clapeyron equation from the CO_2 adsorption isotherms, measured at $T = 273$ and 298 K (Fig. S9†) and at 1 bar pressure. The *df*-TzCTF400 shows the highest Q_{st} value ranging 36–35 kJ mol^{-1}, followed by *df*-TzCTF600, TzCTF400, and TzCTF600 with ranging Q_{st} values of 34–30, 32–25, and 28–24 kJ mol^{-1}, respectively. At zero-loading, the Q_{st} values of all TzCTFs remain between 35 and 28 kJ mol^{-1}, and the values remain almost constant even at high loading, indicating the presence of relatively strong interaction between TzCTFs skeletons and CO_2 molecules. Moreover, the Q_{st} values of TzCTFs over the entire range of CO_2 loading fall in the ideal range (<40 kJ mol^{-1}) for CO_2 storage materials, suggesting lower regeneration cost compared to conventional widely used amine solutions (>40 kJ mol^{-1}). Among the four materials, *df*-TzCTF600 and *df*-TzCTF400 show the highest initial Q_{st} values of 35 and 34 kJ mol^{-1}, respectively, suggesting a stronger affinity for CO_2, compared to TzCTF600 and TzCTF400 materials. The presence of additional narrow ultramicropores (<7 Å) because of defluorination carbonization process during preparation, along with embedded basic CO_2-phillic sites, mainly trioazolic and pyrollic nitrogen species, synergistically gives a rationale to the observed affinity towards CO_2 and, thereby, exceptionally large CO_2 uptake capabilities of *df*-TzCTF600 and *df*-TzCTF400 materials.

For real-life application of TzCTFs as potential CO_2 adsorbents, particularly flue gas adsorbents, competitive CO_2 uptake over N_2 needed to be examined further with regard to their anticipated performance in pressure swing adsorption (PSA) units. The separation of CO_2/N_2 gas mixtures in a PSA unit is commonly carried out in fixed bed adsorbers, in which the separation performance is mainly dictated by a combination of two separate factors: (i) adsorption selectivity and (ii) uptake capacity. For a proper comparison of the performance of *df*-TzCTF600, *df*-TzCTF400, TzCTF600, and TzCTF400, transient breakthrough simulations are conducted that are representative of industrial fixed bed operations under kinetic flowing mixed gas (CO_2/N_2) condition, using a precise methodology developed by Krishna and Long (see ESI† for details). This methodology has a great future potential to identify a vast number of various type of porous materials having the most promising CO_2 separation properties prior to extensive experimental efforts.[106–108] In

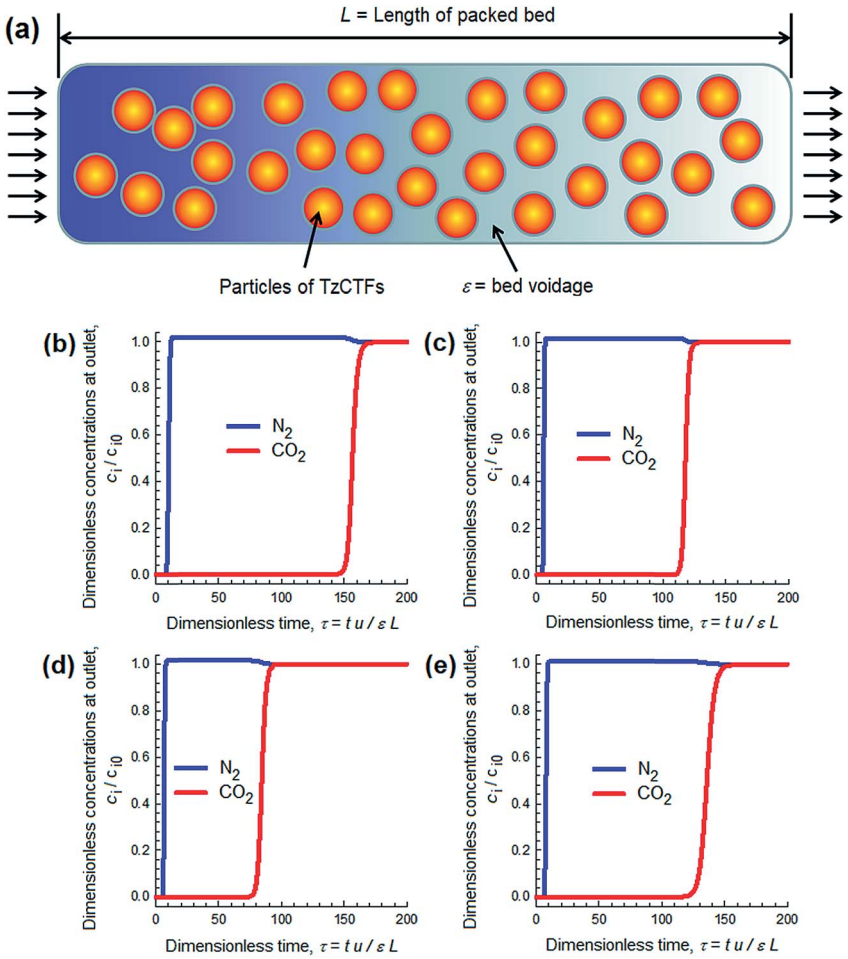

Fig. 10 (a) Schematic of a packed bed adsorber for TzCTFs. CO_2/N_2 mixture breakthrough characteristics of (b) *df*-TzCTF600, (c) *df*-TzCTF400, (d) TzCTF600, and (e) TzCTF400 at 298 K.

a typical experiment, a mixed CO_2/N_2 gas stream comprising 15% CO_2 and 85% N_2 was used at $T = 298$ K under 100 kPa to simulate post-combustion flue gas, following the earlier work of Mason *et al.*[109] Fig. 10 presents typical breakthrough curves for TzCTFs materials, where the *x*-axis is dimensionless time τ, which is derived as the division of the actual time t by the characteristic time $L\varepsilon/\mu$. The *y*-axis in the plot is the concentration of the components in the outlet gas stream, normalized with respect to the inlet composition. A longer breakthrough time for CO_2 indicates better separation performance, because more of CO_2 can be adsorbed in the bed before the need for regeneration. The best separation is achieved with *df*-TzCTF600 because of its high CO_2 uptake capacity in combination with reasonably high CO_2/N_2 adsorption selectivity, and the separation efficiency is comparable to the well-known CTF-based materials, for examples, to those of CTF-1 and CTF-1-600.[55]

Conclusion

In summary, we have introduced two newly designed C3-symmetric 1,2,3-triazole substituted aromatic nitrile building block analogs to prepare a set of novel highly microporous triazole functionalized covalent triazine frameworks (TzCTFs) under $ZnCl_2$ catalyzed ionothermal conditions for high-capacity small gas uptake and separation. Comparative analyses of structure, chemical composition, textural parameters, and gas uptake capabilities of all TzCTFs were comprehensively carried out. Owing to their large surface area, mostly arising from the abundant and dominant narrow- and ultra-micropores along with CO_2-phillic multi-N-containing triazole and triazine embedded pore surfaces, TzCTFs demonstrated exceptionally high CO_2 and H_2 uptake capability. The best uptake was found for *df*-TzCTF600 prepared at 600 °C, utilizing fluorinated precursor with CO_2 uptake capacities of 6.79 mmol g^{-1} (273 K, 1 bar) and 4.6 mmol g^{-1} (298 K, 1 bar). The H_2 storage efficiency was measured to be 2.5 wt%, which ranks among the highest reported to date for related CTF-based materials under identical conditions. Higher CO_2-accessible micropore volume, $V_{micro(CO_2)}$, calculated from CO_2 isotherm ($T = 273$ K), plays a crucial role in enhancing CO_2 uptake at low pressure, compared to the high surface area and microporous volume fractions ($V_{0.1}/V_{tot}$), derived from the N_2 isotherm ($T = 77$ K). Notably, judicious incorporation of thermally labile sacrificial fluorine functionalities into the nitrile building block (Tz-FCN) is one of the most pivotal factors, generating a large degree of ultra-microporosity in the resulting frameworks owing to *in situ* etching process, caused by the release of reactive fluorinated species from the polymer backbone during high temperature polymerization conditions. Moreover, our approach of grafting thermally labile fluorine atom and incorporation of triazole based multi-N-containing hetero-aromatic moiety into the nitrile building block may enable new possibilities for the rational design and synthesis of novel advanced microporous materials for multi task-specific carbon capture and energy storage applications. Along this direction, an extended investigation of the present series of materials is currently ongoing in our research group.

Conflicts of interest

There are no conflicts to declare.

Acknowledgements

S. D. gratefully acknowledges financial and infrastructural support from The Director, CSIR-IMMT and SERB (YSS/2015/001772), New Delhi. S. M. thanks SERB, New Delhi, M. D. acknowledges UGC and A. M. thanks CSIR for their fellowship. S. D. also acknowledges Nabarun Hajra for his help in monomer synthesis and gas adsorption experiments.

References

1 Intergovernmental Panel on Climate Change, *Climate Change 2014: Mitigation of Climate Change. Contribution of Working Group III to the Fifth Assessment Report of the Intergovernmental Panel on Climate Change*, Cambridge University Press, Cambridge, United Kingdom and New York, NY, USA, 2014.
2 IEA, *World Energy Outlook 2018*, IEA, Paris, 2018, DOI: 10.1787/weo-2018-en.
3 IEA, *Energy Technology Perspectives 2017: Catalysing Energy Technology Transformations*, IEA, Paris, 2017, DOI: 10.1787/energy_tech-2017-en.
4 R. S. Haszeldine, *Science*, 2009, **325**, 1647–1652.
5 G. T. Rochelle, *Science*, 2009, **325**, 1652–1654.
6 N. B. McKeown and P. M. Budd, *Chem. Soc. Rev.*, 2006, **35**, 675–683.
7 S. Y. Ding and W. Wang, *Chem. Soc. Rev.*, 2013, **42**, 548–568.
8 W. Lu, D. Yuan, D. Zhao, C. I. Schilling, O. Plietzsch, T. Muller, S. Bräse, J. Guenther, J. Blümel, R. Krishna, Z. Li and H.-C. Zhou, *Chem. Mater.*, 2010, **22**, 5964–5972.
9 W. Lu, Z. Wei, D. Yuan, J. Tian, S. Fordham and H.-C. Zhou, *Chem. Mater.*, 2014, **26**, 4589–4597.
10 L.-B. Sun, A.-G. Li, X.-D. Liu, X.-Q. Liu, D. Feng, W. Lu, D. Yuan and H.-C. Zhou, *J. Mater. Chem. A*, 2015, **3**, 3252–3256.
11 R. L. Martin, C. M. Simon, B. Smit and M. Haranczyk, *J. Am. Chem. Soc.*, 2014, **136**, 5006–5022.
12 L. Tan and B. Tan, *Chem. Soc. Rev.*, 2017, **46**, 3322–3356.
13 Y. Xu, S. Jin, H. Xu, A. Nagai and D. Jiang, *Chem. Soc. Rev.*, 2013, **42**, 8012–8031.
14 J.-X. Jiang, F. Su, A. Trewin, C. D. Wood, N. L. Campbell, H. Niu, C. Dickinson, A. Y. Ganin, M. J. Rosseinsky, Y. Z. Khimyak and A. I. Cooper, *Angew. Chem., Int. Ed.*, 2007, **46**, 8574–8578.
15 T. Ben and S. Qiu, *CrystEngComm*, 2013, **15**, 17–26.
16 L. Huang, X. Yang and D. Cao, *J. Phys. Chem. C*, 2015, **119**, 3260–3267.
17 B. Dutcher, M. Fan and A. G. Russell, *ACS Appl. Mater. Interfaces*, 2015, **7**, 2137–2148.
18 R. J. Notz, I. Tönnies, N. McCann, G. Scheffknecht and H. Hasse, *Chem. Eng. Technol.*, 2011, **34**, 163–172.
19 S. Wu, S. Gu, A. Zhang, G. Yu, Z. Wang, J. Jian and C. Pan, *J. Mater. Chem. A*, 2015, **3**, 878–885.

20 K. Park, K. Lee, H. Kim, V. Ganesan, K. Cho, S. K. Jeong and S. Yoon, *J. Mater. Chem. A*, 2017, **5**, 8576–8582.
21 S. Hug, M. B. Mesch, H. Oh, N. Popp, M. Hirscher, J. Senker and B. V. Lotsch, *J. Mater. Chem. A*, 2014, **2**, 5928–5936.
22 P. Katekomol, J. Roeser, M. Bojdys, J. Weber and A. Thomas, *Chem. Mater.*, 2013, **25**, 1542–1548.
23 X. Zhu, C. Tian, G. M. Veith, C. W. Abney, J. Dehaudt and S. Dai, *J. Am. Chem. Soc.*, 2016, **138**, 11497–11500.
24 C. Gu, D. Liu, W. Huang, J. Liu and R. Yang, *Polym. Chem.*, 2015, **6**, 7410–7417.
25 A. Bhunia, I. Boldog, A. Möller and C. Janiak, *J. Mater. Chem. A*, 2013, **1**, 14990–14999.
26 A. Bhunia, V. Vasylyeva and C. Janiak, *Chem. Commun.*, 2013, **49**, 3961–3963.
27 Y. Liu, S. Wu, G. Wang, G. Yu, J. Guan, C. Pan and Z. Wang, *J. Mater. Chem. A*, 2014, **2**, 7795–7801.
28 Y. Wang, J. Li, Q. Yang and C. Zhong, *ACS Appl. Mater. Interfaces*, 2016, **8**, 8694–8701.
29 H. S. Jena, C. Krishnaraj, G. Wang, K. Leus, J. Schmidt, N. Chaoui and P. Van Der Voort, *Chem. Mater.*, 2018, **30**, 4102–4111.
30 K. Kamiya, R. Kamai, K. Hashimoto and S. Nakanishi, *Nat. Commun.*, 2014, **5**, 5040.
31 K. Kamiya, T. Tatebe, S. Yamamura, K. Iwase, T. Harada and S. Nakanishi, *ACS Catal.*, 2018, **8**, 2693–2698.
32 J. Xie, S. A. Shevlin, Q. Ruan, S. J. A. Moniz, Y. Liu, X. Liu, Y. Li, C. C. Lau, Z. X. Guo and J. Tang, *Energy Environ. Sci.*, 2018, **11**, 1617–1624.
33 T. Wang, K. Kailasam, P. Xiao, G. Chen, L. Chen, L. Wang, J. Li and J. Zhu, *Microporous Mesoporous Mater.*, 2014, **187**, 63–70.
34 K. Leus, K. Folens, N. R. Nicomel, J. P. H. Perez, M. Filippousi, M. Meledina, M. M. Dîrtu, S. Turner, G. V. Tendeloo, Y. Garcia, G. D. Laing and P. Van Der Voort, *J. Hazard. Mater.*, 2018, **353**, 312–319.
35 Y. Li, S. Zheng, X. Liu, P. Li, L. Sun, R. Yang, S. Wang, Z. -S. Wu, X. Bao and W. -Q. Deng, *Angew. Chem., Int. Ed.*, 2018, **57**, 7992–7996.
36 L. Hao, B. Luo, X. Li, M. Jin, Y. Fang, Z. Tang, Y. Jia, M. Liang, A. Thomas, J. Yang and L. Zhi, *Energy Environ. Sci.*, 2012, **5**, 9747–9751.
37 L.-M. Tao, F. Niu, D. Zhang, T.-M. Wang and Q.-H. Wang, *New J. Chem.*, 2014, **38**, 2774–2777.
38 H. Deng, H. Yi, X. Tang, Q. Yu, P. Ning and L. Yang, *Chem. Eng. J.*, 2012, **188**, 77–85.
39 J. Zhang, R. Singh and P. A. Webley, *Microporous Mesoporous Mater.*, 2008, **111**, 478–487.
40 K. Sumida, D. L. Rogow, J. A. Mason, T. M. McDonald, E. D. Bloch, Z. R. Herm, T. H. Bae and J. R. Long, *Chem. Rev.*, 2012, **112**, 724–781.
41 J.-R. Li, Y. Ma, M. C. McCarthy, J. Sculley, J. Yu, H.-K. Jeong, P. B. Balbuena and H.-C. Zhou, *Coord. Chem. Rev.*, 2011, **255**, 1791–1823.
42 Y. Liu, Z. U. Wang and H.-C. Zhou, *Greenhouse Gases: Sci. Technol.*, 2012, **2**, 239–259.
43 M. Sevilla and A. B. Fuertes, *Energy Environ. Sci.*, 2011, **4**, 1765–1771.
44 A. S. Jalilov, G. Ruan, C.-C. Hwang, D. E. Schipper, J. J. Tour, Y. Li, H. Fei, E. L. G. Samuel and J. M. Tour, *ACS Appl. Mater. Interfaces*, 2015, **7**, 1376–1382.
45 J. Yang, L. Yue, X. Hu, L. Wang, Y. Zhao, Y. Lin, Y. Sun, H. DaCosta and L. Guo, *Energy Fuels*, 2017, **31**, 4287–4293.
46 J. Chen, J. Yang, G. Hu, X. Hu, Z. Li, S. Shen, M. Radosz and M. Fan, *ACS Sustainable Chem. Eng.*, 2016, **4**, 1439–1445.
47 K. Sim, N. Lee, J. Kim, E.-B. Cho, C. Gunathilake and M. Jaroniec, *ACS Appl. Mater. Interfaces*, 2015, **7**, 6792–6802.
48 R. Sanz, G. Calleja, A. Arencibia and E. S. Sanz-Pérez, *Appl. Surf. Sci.*, 2010, **256**, 5323–5328.
49 S. Hao, H. Chang, Q. Xiao, Y. Zhong and W. Zhu, *J. Phys. Chem. C*, 2011, **115**, 12873–12882.
50 P. Kuhn, M. Antonietti and A. Thomas, *Angew. Chem., Int. Ed.*, 2008, **47**, 3450–3453.
51 S. Dey, A. Bhunia, H. Breitzke, P. B. Groszewicz, G. Buntkowsky and C. Janiak, *J. Mater. Chem. A*, 2017, **5**, 3609–3620; S. Dey, A. Bhunia, I. Boldog and C. Janiak, *Microporous Mesoporous Mater.*, 2017, **241**, 303–315.
52 S. Hug, M. E. Tauchert, S. Li, U. E. Pachmayr and B. V. Lotsch, *J. Mater. Chem.*, 2012, **22**, 13956–13964.
53 Y. J. Lee, S. N. Talapaneni and A. Coskun, *ACS Appl. Mater. Interfaces*, 2017, **9**, 30679–30685.
54 P. Kuhn, A. Thomas and M. Antonietti, *Macromolecules*, 2009, **42**, 319–326.
55 Y. Zhao, K. X. Yao, B. Teng, T. Zhang and Y. Han, *Energy Environ. Sci.*, 2013, **6**, 3684–3692.
56 S. Hug, L. Stegbauer, H. Oh, M. Hirscher and B. V. Lotsch, *Chem. Mater.*, 2015, **27**, 8001–8010.
57 G. Wang, K. Leus, H. S. Jena, C. Krishnaraj, S. Zhao, H. Depauw, N. Tahir, Y.-Y. Liu and P. Van Der Voort, *J. Mater. Chem. A*, 2018, **6**, 6370–6375.
58 M. R. Liebl and J. Senker, *Chem. Mater.*, 2013, **25**, 970–980.
59 H. M. Lee, I. S. Youn, M. Saleh, J. W. Lee and K. S. Kim, *Phys. Chem. Chem. Phys.*, 2015, **17**, 10925–10933.
60 X.-M. Hu, Q. Chen, Y.-C. Zhao, B. W. Laursen and B.-H. Han, *J. Mater. Chem. A*, 2014, **2**, 14201–14208.
61 M. Meldal and C. W. Tornøe, *Chem. Rev.*, 2008, **108**, 2952–3015.
62 S. Wu, Y. Liu, G. Yu, J. Guan, C. Pan, Y. Du, X. Xiong and Z. Wang, *Macromolecules*, 2014, **47**, 2875–2882.
63 J. Jia, Z. Chen, Y. Belmabkhout, K. Adil, P. M. Bhatt, V. A. Solovyeva, O. Shekhah and M. Eddaoudi, *J. Mater. Chem. A*, 2018, **6**, 15564–15568.
64 M. Saleh, S. B. Baek, H. M. Lee and K. S. Kim, *J. Phys. Chem. C*, 2015, **119**, 5395–5402.
65 J.-M. Gu, W.-S. Kim, Y.-K. Hwang and S. Huh, *Carbon*, 2013, **56**, 208–217.
66 P. Pandey, O. K. Farha, A. M. Spokoyny, C. A. Mirkin, M. G. Kanatzidis, J. T. Hupp and S. T. Nguyen, *J. Mater. Chem.*, 2011, **21**, 1700–1703.
67 H. Zhong, C. Liu, Y. Wang, R. Wang and M. Hong, *Chem. Sci.*, 2016, **7**, 2188–2194.
68 H. Zhong, Y. Gong, F. Zhang, L. Li and R. Wang, *J. Mater. Chem. A*, 2014, **2**, 7502–7508.
69 X. Zhu, S. M. Mahurin, S.-H. An, C.-L. Do-Thanh, C. Tian, Y. Li, L. W. Gill, E. W. Hagaman, Z. Bian, J.-H. Zhou,

J. Hu, H. Liu and S. Dai, *Chem. Commun.*, 2014, **50**, 7933–7936.
70 X. Liu, H. Li, Y. Zhang, B. Xu, A. Sigen, H. Xia and Y. Mu, *Polym. Chem.*, 2013, **4**, 2445–2448.
71 M. J. Bojdys, J. Jeromenok, A. Thomas and M. Antonietti, *Adv. Mater.*, 2010, **22**, 2202–2205.
72 Z. Q. Li, C. J. Lu, Z. P. Zia, Y. Zhou and Z. Luo, *Carbon*, 2007, **45**, 1686–1695.
73 P. Zhang, Y. Gong, H. Li, Z. Chen and Y. Wang, *Nat. Commun.*, 2013, **4**, 1593.
74 A. C. Ferrari and J. Robertson, *Phys. Rev. B: Condens. Matter Mater. Phys.*, 2001, **64**, 075414.
75 J. H. Kaufman and S. Metin, *Phys. Rev. B: Condens. Matter Mater. Phys.*, 1989, **39**, 13053–13060.
76 S. N. Talapaneni, J. H. Lee, S. H. Je, O. Buyukcakir, T. Kwon, K. Polychronopoulou, J. W. Choi and A. Coskun, *Adv. Funct. Mater.*, 2017, **27**, 1604658.
77 P. Kuhn, A. Forget, D. Su, A. Thomas and M. Antonietti, *J. Am. Chem. Soc.*, 2008, **130**, 13333–13337.
78 P. Kuhn, A. Forget, J. Hartmann, A. Thomas and M. Antonietti, *Adv. Mater.*, 2009, **21**, 897–901.
79 B. Marchon, J. Carrazza, H. Heinemann and G. A. Somorjai, *Carbon*, 1988, **26**, 507–514.
80 G. Chen, X. Wang, J. Li, W. Hou, Y. Zhou and J. Wang, *ACS Appl. Mater. Interfaces*, 2015, **7**, 18508–18518.
81 V. León, M. Quintana, M. A. Herrero, J. L. G. Fierro, A. de la Hoz, M. Prato and E. Vázquez, *Chem. Commun.*, 2011, **47**, 10936–10938.
82 D. Y. Osadchii, A. I. Olivos-Suarez, A. V. Bavykina and J. Gascon, *Langmuir*, 2017, **33**, 14278–14285.
83 S. Ciampi, T. Böcking, K. A. Kilian, M. James, J. B. Harper and J. J. Gooding, *Langmuir*, 2007, **23**, 9320–9329.
84 K. S. W. Sing, D. H. Everett, R. A. W. Haul, L. Moscou, R. A. Pierotti, J. Rouquerol and T. Siemieniewska, *Pure Appl. Chem.*, 1985, **57**, 603–619.
85 M. Thommes, B. Smarsly, M. Groenewolt, P. I. Ravikovitch and A. V. Neimark, *Langmuir*, 2006, **22**, 756–764.
86 S. Brunauer, P. H. Emmett and E. Teller, *J. Am. Chem. Soc.*, 1938, **60**, 309–319.
87 R. Dawson, A. Laybourn, R. Clowes, Y. Z. Khimyak, D. J. Adams and A. I. Cooper, *Macromolecules*, 2009, **42**, 8809–8816.
88 J. Garrido, A. Linares-Solano, J. M. Martin-Martinez, M. Molina-Sabio, F. Rodriguez-Reinoso and R. Torregrosa, *Langmuir*, 1987, **3**, 76–81.
89 F. Rodriguez-Reinoso and A. Linares-Solano, in *Chemistry and Physics of Carbon*, ed. P. A. Thrower, Marcel Dekker, New York, 1988, vol. 21, pp. 1–146.
90 M. Thommes, K. Kaneko, A. V. Neimark, J. P. Olivier, F. Rodriguez-Reinoso, J. Rouquerol and K. S. W. Sing, *Pure Appl. Chem.*, 2015, **87**, 1051–1069.
91 K. Kaneko, N. Setoyama and T. Suzuki, in *Characterization of Porous Solids III*, ed. J. Rouquerol, *et al.*, Elsevier Science Publishers B.V., Amsterdam, 1994, p. 593.
92 D. Cazorla-Amorós, J. Alcañiz-Monge and A. Linares-Solano, *Langmuir*, 1996, **12**, 2820–2824.
93 J. Garcia-Martinz, D. Cazorla-Amorós and A. Linares-Solano, in *Characterization of Porous Solids V*, ed. K. K. Unger, G. Kreysa and J. P. Baselt, Elsevier, Amsterdam, 2000, vol. 128, pp. 485–494.
94 Y. He, W. Zhou, G. Qian and B. Chen, *Chem. Soc. Rev.*, 2014, **43**, 5657–5678.
95 G. Tuci, M. Pilaski, H. Ba, A. Rossin, L. Luconi, S. Caporali, C. Pham-Huu, R. Palkovits and G. Giambastiani, *Adv. Funct. Mater.*, 2017, **27**, 1605672.
96 Y. Zhu, H. Long and W. Zhang, *Chem. Mater.*, 2013, **25**, 1630–1635.
97 Y. H. Abdelmoaty, T.-D. Tessema, F. A. Choudhury, O. M. El-Kadri and H. M. El-Kaderi, *ACS Appl. Mater. Interfaces*, 2018, **10**, 16049–16058.
98 T. C. Drage, C. E. Snape, L. A. Stevens, J. Wood, J. Wang, A. I. Cooper, R. Dawson, X. Guo, C. Satterley and R. Irons, *J. Mater. Chem.*, 2012, **22**, 2815–2823.
99 R. Dawson, L. A. Stevens, T. C. Drage, C. E. Snape, M. W. Smith, D. J. Adams and A. I. Cooper, *J. Am. Chem. Soc.*, 2012, **134**, 10741–10744.
100 A. C. Kizzie, A. G. Wong-Foy and A. J. Matzger, *Langmuir*, 2011, **27**, 6368–6373.
101 G. Li, B. Zhang, J. Yan and Z. Wang, *Macromolecules*, 2014, **47**, 6664–6670.
102 W. Lu, D. Yuan, J. Sculley, D. Zhao, R. Krishna and H.-C. Zhou, *J. Am. Chem. Soc.*, 2011, **133**, 18126–18129.
103 P. Mohanty, L. D. Kull and K. Landskron, *Nat. Commun.*, 2011, **2**, 401.
104 Q. Chen, M. Luo, P. Hammershøj, D. Zhou, Y. Han, B. W. Laursen, C.-G. Yan and B.-H. Han, *J. Am. Chem. Soc.*, 2012, **134**, 6084–6087.
105 H. A. Patel, S. H. Je, J. Park, D. P. Chen, Y. Jung, C. T. Yavuz and A. Coskun, *Nat. Commun.*, 2013, **4**, 1357.
106 R. Krishna and J. R. Long, *J. Phys. Chem. C*, 2011, **115**, 12941–12950.
107 R. Krishna, *Microporous Mesoporous Mater.*, 2014, **185**, 30–50.
108 R. Krishna, *RSC Adv.*, 2015, **5**, 52269–52295.
109 A. J. Mason, K. Sumida, Z. R. Herm, R. Krishna and J. R. Long, *Energy Environ. Sci.*, 2011, **4**, 3030–3040.

Electronic Supporting Information (ESI)

Newly Designed 1,2,3-Triazole Functionalized Covalent Triazine Frameworks with Exceptionally High Uptake Capacity of both CO_2 and H_2

Soumya Mukherjee,[ab] Monojit Das,[ab] Anupam Manna,[ab] Rajamani Krishna,[c] and Sanjib Das*[,ab]

[a]Department of Colloids & Materials Chemistry, CSIR-Institute of Minerals & Materials Technology, Bhubaneswar 751013, Odisha, India. Email: sanjibdas@immt.res.in

[b]Academy of Scientific & Innovative Research (AcSIR), Ghaziabad 201002, India.

[c]Van't Hoff Institute for Molecular Sciences, University of Amsterdam, Science Park 904, 1098 XH Amsterdam, The Netherlands.

Section A. Materials and methods:

All chemical reagents were purchased from commercial sources and used as received unless otherwise stated. Periodic acid, dimethylamino pyridine, ammonium formate, potassium iodide, triethylamine, $CuSO_4.5H_2O$, cesium fluoride, and sodium thiosulfate were purchased from Spectrochem (India). 1,3,5-trifluorobenzene, (trimethylsilyl)acetylene, tetrakis(triphenylphosphine)palladium(0), Pd/C, 5-nitroisophthalic acid, DCC, and sodium ascorbate were purchased from Alfa Aesar. Anhydrous zinc chloride was purchased from Alfa-Aesar and further dried at 110 ^{0}C under vacuum prior to use. All organic solvents were procured from Spectrochem (India). Anhydrous THF was prepared by continuously refluxing THF over sodium and freshly distilled under argon. Column chromatography was performed using silica gel purchased from Spectrochem (India).

Solution **^{1}H, and ^{19}F NMR spectra** were recorded on a Bruker® Ultrashield instrument operating at a frequency of 400 MHz with tetramethylsilane (TMS) as an internal standard using $CDCl_3$ as solvent. All measurements were carried out at ambient temperature and chemical shifts are reported in parts per million (ppm) relative to the deuterated solvent. **Solid state cross polarization magic angle spinning (CP-MAS) ^{13}C NMR** was performed at ambient temperature on JEOL JNM-ECX400II solid-state NMR spectrometer operating at a frequency of 400 MHz. **Fourier-transform Infrared spectra (FT-IR)** of starting materials and as-synthesized TzCTFs were obtained using a Perkin Elmer Spectrum-GX spectrophotometer with KBr pallet in transmittance mode. All FT-IR spectra were background corrected. **Powder X-ray diffraction (PXRD)** patterns were recorded on a Rigaku Ultima-IV diffractometer using monochromated Cu-K_α (λ = 1.54060 Å) radiation with a scan speed of 2° min^{-1} and a step size of 0.01° in 2θ. The X-ray tube operated at a voltage of 40 kV and a current of 30 mA. Thermogravimetric analyses were carried out in a nitrogen stream using Netzsch STA 449F3-jupiter thermogravimetric-differential scanning calorimetry (TG-DSC) analyzer with a heating rate of 10 °C/min. **The Raman spectra** were measured on a Horiba LabRAM HR confocal micro-Raman system with excitation source of 532 nm diode-pumped solid state laser. **Field emission scanning electron microscopy (FE-SEM)** images were taken using Carl Zeiss AG Supra Gemini 55 at an accelerating voltage of 15 kV and equipped with OXFORD energy dispersive X-ray spectrometer. The powder samples were dispersed in ethanol and the suspension was drop casted on a clean piece of silicon wafer. **High-resolution Transmission electron microscopy (TEM)** images were captured using field-emission JEOL, JEM-2100F at an accelerating voltage of 200 kV. The

powder samples were dispersed in dichloromethane (DCM) and one drop of the suspension was drop casted on a carbon coated copper grid. **Elemental analysis** (C, H, and N) were performed on a Thermo Scientific Flash 2000 Organic Elemental Analyzer. **High resolution X-ray photoelectron spectroscopy (XPS)** spectra were recorded with PHI 5000 Versa Probe II XPS with AES module comprising argon ion as well as C60 sputter guns. All **low pressure gas adsorption-desorption experiments** (up to 1 bar) were carried out on Quantachrome Autosorb-iQ surface area & pore size analyzer. Before gas adsorption experiment sample was degassed first at 140^0C under a dynamic vacuum for 12 hours. High-purity-grade He, N_2, H_2, CO_2 and CH_4 gases were used in all adsorption measurements. N_2 (77 K) and H_2 (77 K) isotherms were measured using a liquid nitrogen bath. CO_2 N_2, and CH_4 isotherms at variable temperatures (from 273 K to 308 K) were measured using a jacketed recirculating dewar containing mixed water and ethylene glycol (1:1 ratio) and the dewar was connected to a chiller (JULABO, FL300, working temperature range: -20 to +40°C, temperature stability: ±0.5°C) having circulating methanol to precisely achieve analysis temperature 308 K, 298 K, and 273 K, respectively. The Brunauer-Emmett-Teller (BET) surface area was calculated over the relative pressure range 0.05 – 0.3 P/P_0 whereas Langmuir surface area calculated taking relative pressure range 0 – 0.15 P/P_0. Total pore volumes were measured at relative pressure near 0.99 P/P_0 while microporosity was estimated by measuring the pore volume at a relative pressure of 0.1 P/P_0. Pore size distributions and pore volumes were derived from the isotherms using the non-local density functional theory (NL-DFT) slit pore model on carbon.

Section B. General Synthetic Procedures:

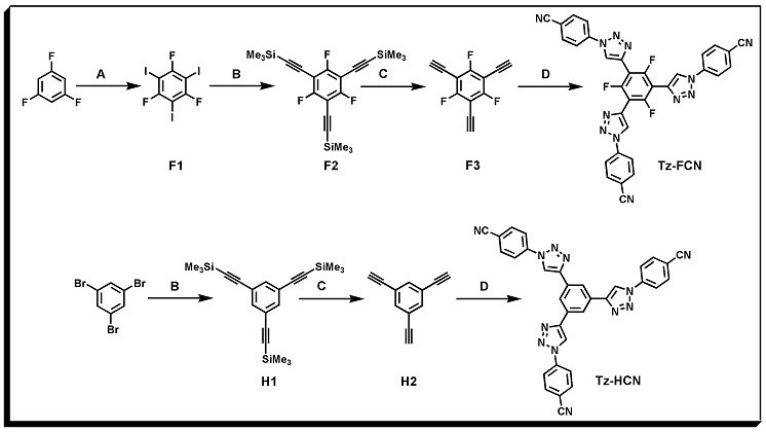

A: $HIO_4.2H_2O$, $Conc.H_2SO_4$, Finely ground KI, 70°C, 6 hours; **B**: Trimethylsilylacetylene, CuI, $Pd(PPh_3)_4$, THF, Triethylamine, 90°C, 12 hrs; **C**: CsF, Ethanol, Tetrahydrofuran, 50 min, RT; **D:** 4-Azidobenzonitrile, Sodium ascorbate, Water, Tetrahydrofuran, 40°C, 3 days.

Scheme S1: Synthetic route of Tz-FCN and Tz-HCN building blocks

Synthetic Procedures:

1,3,5-trifluoro-2,4,6-triiodobenzene (F1):[S1] A 100 ml round bottom flask equipped with stir bar was charged with 25 ml conc. H_2SO_4 and the flask was cooled down to 0^{o}C using an ice-bath. Then $HIO_4.2H_2O$ (3.88 g, 17.03 mmol) was added into the mixture over 15 minutes followed by addition of finely grounded KI (8.51 g, 51.27 mmol) in small portions over 10 mins. 1,3,5-trifluorobenzene (1.5 g, 11.3 mmol) was added dropwise via a syringe and the mixture was stirred for 10 minutes while the temperature was held at 0^{o}C. The ice-bath was removed and the reaction mixture was at 70^{o}C for an additional 6 hours. After completion of reaction, the mixture was cooled down to room temperature and poured into crushed ice while stirring. The mixture was extracted with diethyl ether (3 x 50ml) and the combined organic layer was washed by saturated solution of sodium thiosulfate (2x50 ml), water and dried over anhydrous $MgSO_4$. The organic layer was evaporated to dryness to afford **F1** as off white colored solid almost quantitatively. The product is directly used in next step without any further purification.

1,3,5-trifluoro-2,4,6-tris[(trimethylsilyl)ethynyl)]benzene (F2):[S2] A 250 ml two neck round bottom flask equipped with stir bar was charged with 1,3,5-trifluoro-2,4,6-triiodobenzene (1.5 g, 2.94 mmol), CuI (60 mg, 0.294 mmol), and tetrakis(triphenylphosphine)palladium(0) (340 mg, 0.29 mmol), anhydrous THF (40 ml), and freshly distilled triethylamine (40 ml) under argon atmosphere. The reaction mixture was stirred for 30 mins at room temperature followed by dropwise addition of trimethylsilylacetylene (1.21 g, 12 mmol). The mixture was heated at 90^{o}C under inert condition for an additional 12 hours. After completion of reaction, the reaction mixture was cooled down to room temperature, filtered and extracted by dichloromethane (3 x 50 ml). The combined organic layer was washed with water and dried over anhydrous $MgSO_4$. The organic layer was evaporated to dryness under reduced pressure. The crude product was purified by silica gel column chromatography (hexane) yielding 1,3,5-trifluoro-2,4,6-tris[(trimethylsilyl)ethynyl)]benzene (**F2**) (915 mg, 85 %) as white colored solid. ^{1}H NMR (400 MHz; $CDCl_3$): 0.26 (s, 27H).

1,3,5-triethynyl-2,4,6-trifluorobenzene (F3):[S3] A 50 ml round bottom flask equipped with stir bar was charged with 1,3,5-trifluoro-2,4,6-tris[(trimethylsilyl)ethynyl)]benzene **F2** (915 mg, 2.17 mmol), 14 ml of THF, and 7 ml of ethanol followed by addition of CsF (1.04 g, 6.84 mmol). The reaction mixture was stirred for 50 minutes at RT under inert condition. The solvent was evaporated under reduced pressure and the crude product was purified by silica

gel column chromatography (hexane:dichloromethane 9:1) yielding **F3** (205 mg, 55 %) as white colored solid. ^{1}H NMR (400 MHz; $CDCl_3$): 3.53 (s, 3H).

Synthesis of Tz-FCN: A 250 ml round bottom flask equipped with stir bar was charged with 1,3,5-triethynyl-2,4,6-trifluorobenzene (200 mg, 0.98 mmol), 4-azidobenzonitrile (510 mg, 3.39 mmol), THF (75 ml), and water (30 ml). The resulting clear solution was purged with argon over 30 min at room temperature followed by addition of $CuSO_4.5H_2O$ (81 mg, 0.31 mmol) and sodium ascorbate (119 mg, 0.60 mmol). The reaction mixture was heated to 40^{o}C and kept stirring for 3 days under inert atmosphere. The bright yellow precipitate was filtered and washed several times with DMSO, Water, Methanol, DCM, and Acetone, respectively, and finally dried in vacuum oven at 70^{o}C resulting **Tz-FCN** (61% yield; Mp 194 ^{o}C) as bright yellow colored solid. The titled compound (**Tz-FCN**) is almost insoluble in all common organic solvents. Solid-state ^{13}C NMR (ppm): 156, 141, 131, 120, 112, 107; IR (KBr pellet, cm^{-1}): 2230, 1607, 1515, 1460, 1400, 1236, 1080, 1039, 987, 841, 735, 551.

1,3,5-tris[2-(trimethylsilyl)ethynyl]benzene (H1):[S2] A 250 ml two neck round bottom flask equipped with stir bar was charged with 1,3,5-tribromobenzne (6.0 g, 19.05 mmol), CuI (145.12 mg, 0.762 mmol), PPh_3 (999.32 mg, 3.81 mmol), $PdCl_2(PPh_3)_2$ (668.56 mg, 0.95 mmol), anhydrous THF (60 ml), and diisopropyl amine (60 ml). The mixture was purged with argon over 10 mins at room temperature followed by dropwise addition of trimethylsilylacetylene (6.74 g, 19.05 mmol) under inert condition. The reaction mixture was heated to 70^{o}C for overnight and cooled down to room temperature. The mixture was filtered and the filtrate was extracted by chloroform (3 x 50 ml) and washed with water and then dried over anhydrous $MgSO_4$. Organic layer was evaporated to dryness and the crude product was purified via column chromatography (silica gel, hexane) to obtain cream colored solid compound (5.3 g, 80%). ^{1}H NMR (400 MHz; $CDCl_3$): 0.23 (s, 27H), 7.49 (s, 3H).

1,3,5-triethynylbenzene (H2):[S4] A 100 ml round bottom flask equipped with stir bar was charged with 1,3,5-tris(2-(trimethylsilyl)ethynyl)benzene (2.0 g, 5.45 mmol) and methanol (60 ml) followed by addition of K_2CO_3 (4.51 g, 32.70). The clear reaction mixture was stirred at room temperature for 6 hours. After completion of reaction, mixture was filtered and solvent was evaporated to dryness. The crude product was purified by column chromatography (silica gel, hexane) to afford the title compound (750 mg, 91.6% yield). ^{1}H NMR (400 MHz; $CDCl_3$): 3.11 (s, 3H), 7.57 (s, 3H).

Synthesis of Tz-HCN: The title compound was synthesized adopting the above mentioned procedure for Tz-FCN using 1,3,5-triethynylbenzene (200 mg, 0.9797 mmol) as starting material resulting yellow colored compound (55.4% yield; Mp 174 ^{o}C). The titled compound

(**Tz-HCN**) is almost insoluble in all common organic solvents. Solid-state ^{13}C NMR (ppm): 146, 139, 131, 121, 111; IR (KBr pellet, cm^{-1}): 2230, 1607, 1515, 1400, 1236, 1039, 987, 840, 551; Anal. Calcd for $C_{33}H_{18}N_{12}$: C, 68.03; H, 3.11; N, 28.85. Found: C, 66.79; H, 3.05; N, 29.41.

Synthesis of 4-azido benzonitrile:[S5] A 100 ml round bottom flask equipped with stir bar was charged with 4-aminobenzonitrile (1.18 g, 10 mmol), p-toluenesulfonic acid monohydrate (5.16 g, 30 mmol), and acetonitrile (40 ml). The reaction mixture was cooled down to 0-5^{0}C and stirred for 1 hour. Ice-cold 6.0 ml sodium nitrite (1.38 g, 20 mmol) solution was added dropwise into the reaction mixture and stirring was continued for 30 min and then solid sodium azide (1.04 g, 16 mmol) was added and the mixture was stirred for an addition 1.0 hour at 10^{o}C. The reaction mixture was then allowed to room temperature followed by extraction with chloroform (3x25 ml). The chloroform layer was washed by water (3x100 ml) followed by drying the organic part over anhydrous $MgSO_4$. The organic layer was evaporated to dryness under reduced pressure using rotary evaporator. The crude product was purified by column chromatography (silica gel, chloroform: hexane = 3:2) to obtain the title compound (1.01 g, 82%). ^1H NMR (400 MHz; DMSO-d_6): 7.25 (d, 2H), 7.78 (d, 2H).

Section C. FT-IR Spectroscopy:

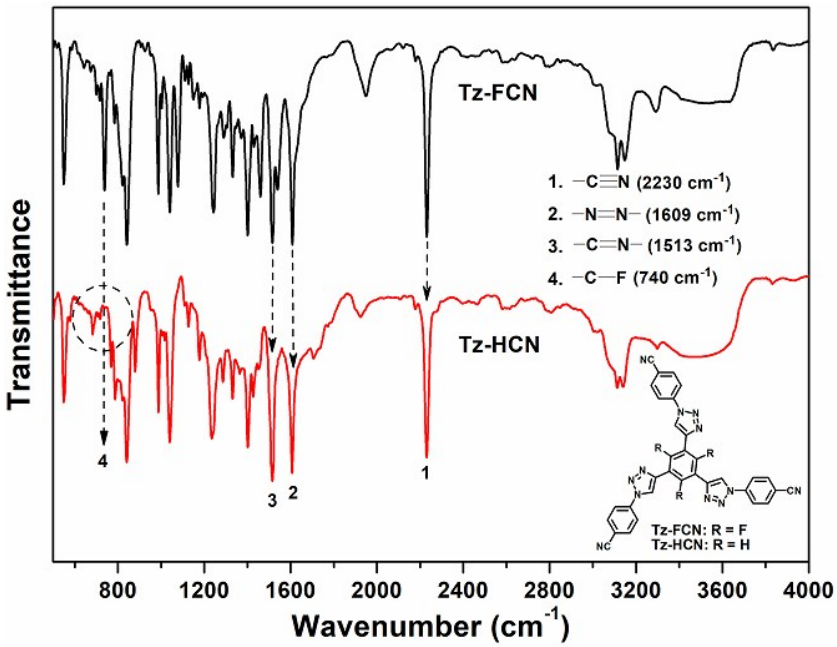

Figure S1: FT-IR spectra of Tz-FCN and TzHCN building blocks

Section D. Solid-State ^{13}C CP-MAS NMR Spectroscopy:

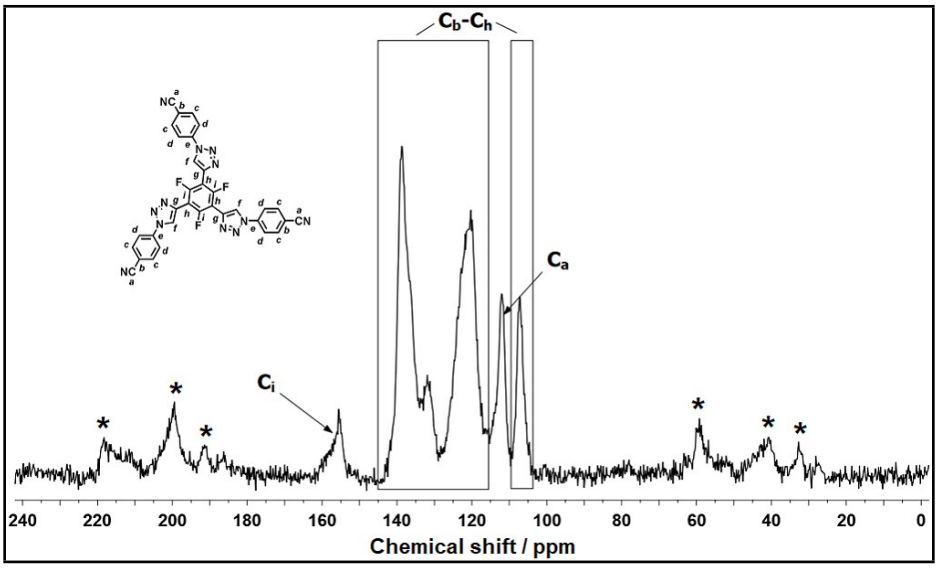

Figure S2: Solid-state ^{13}C CP/MAS NMR spectrum of Tz-FCN building block. Spinning side bands are starred.[S6]

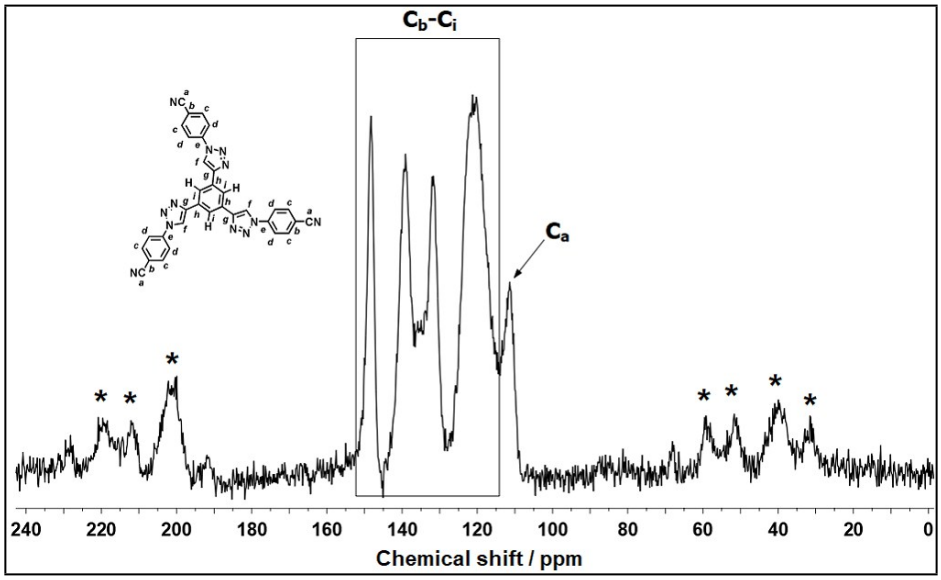

Figure S3: Solid-state ^{13}C CP/MAS NMR spectrum of Tz-HCN building block. Spinning side bands are starred.[S6]

Section E. Powder X-ray diffraction analysis:

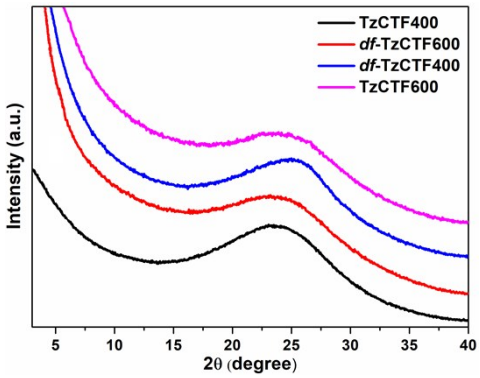

Figure S4: Powder X-ray diffraction spectra of all TzCTF materials.

Section F. Elemental analysis:

Table S1. Elemental analysis of TzCTFs materials from combustion process

Sample	Elemental Analysis (Experimental)			C/N	C/H
	C	N	H		
TzCTF400	69.17	7.89	2.61	8.76	26.50
TzCTF600	67.56	7.05	2.16	9.58	31.15
df-TzCTF400	63.24	8.97	2.13	7.05	29.70
df-TzCTF600	60.83	8.26	2.01	7.36	28.29
Calc. Tz-HCN	68.03	28.85	3.11	2.35	21.87

Section G. XPS survey scan:

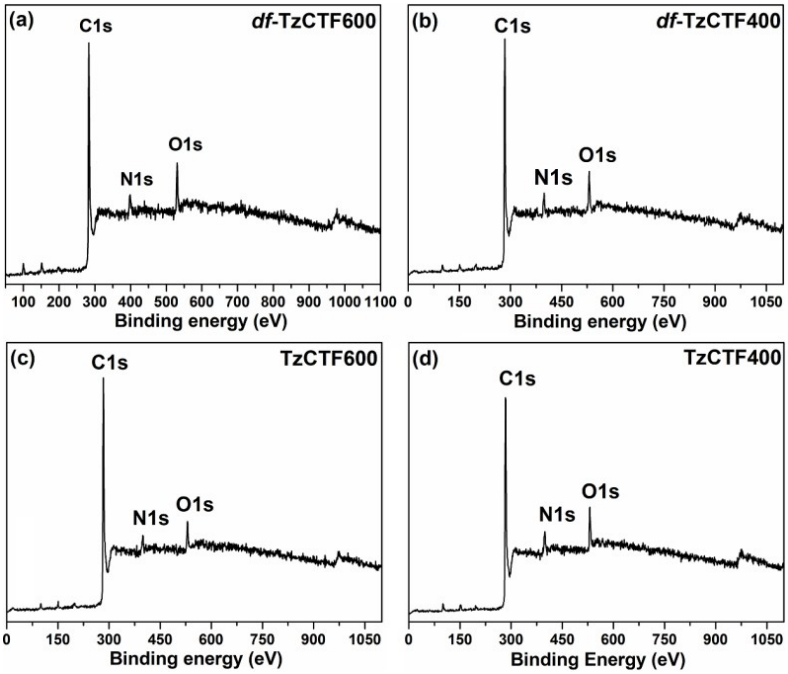

Figure S5: XPS survey spectra (a–d) of TzCTFs

Section H. Pure component isotherms of N_2 and CH_4:

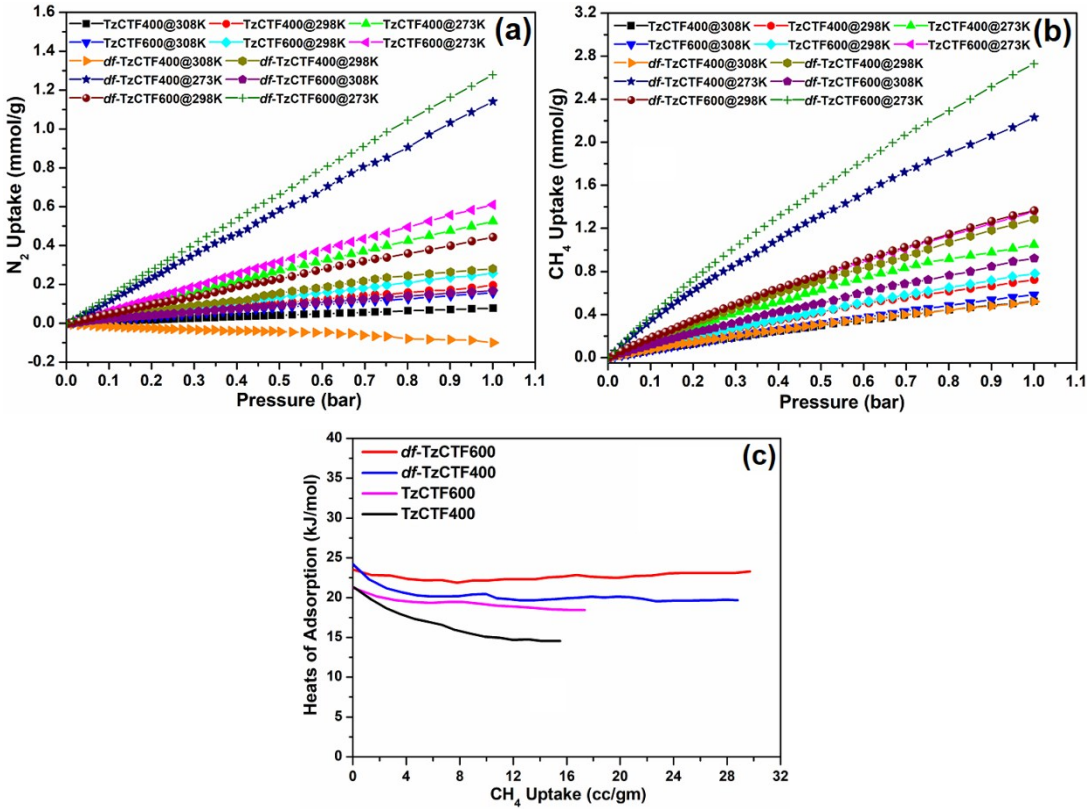

Figure S6: (a) N_2 adsorption, (b) CH_4 adsorption of TzCTF series measure at 273 K, 298 K, and 308 K under 1 bar and (c) Isosteric heat of adsorption for TzCTFs derived from CH_4 adsorption isotherms at 273 K and 298 K

Section I. Henry plots for CO_2, N_2, and CH_4:

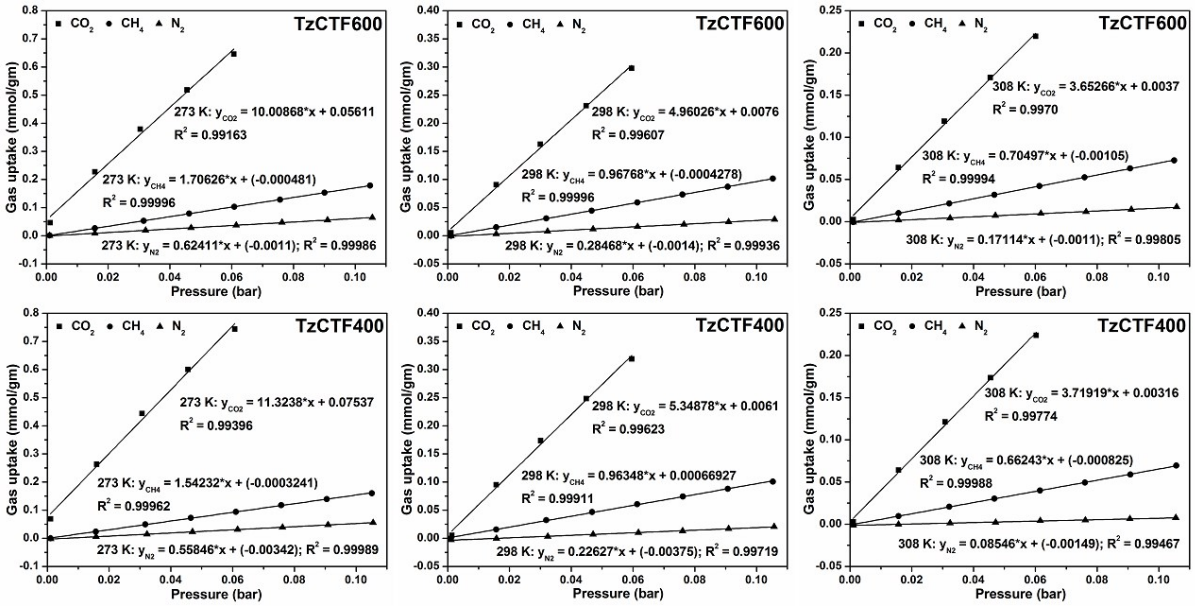

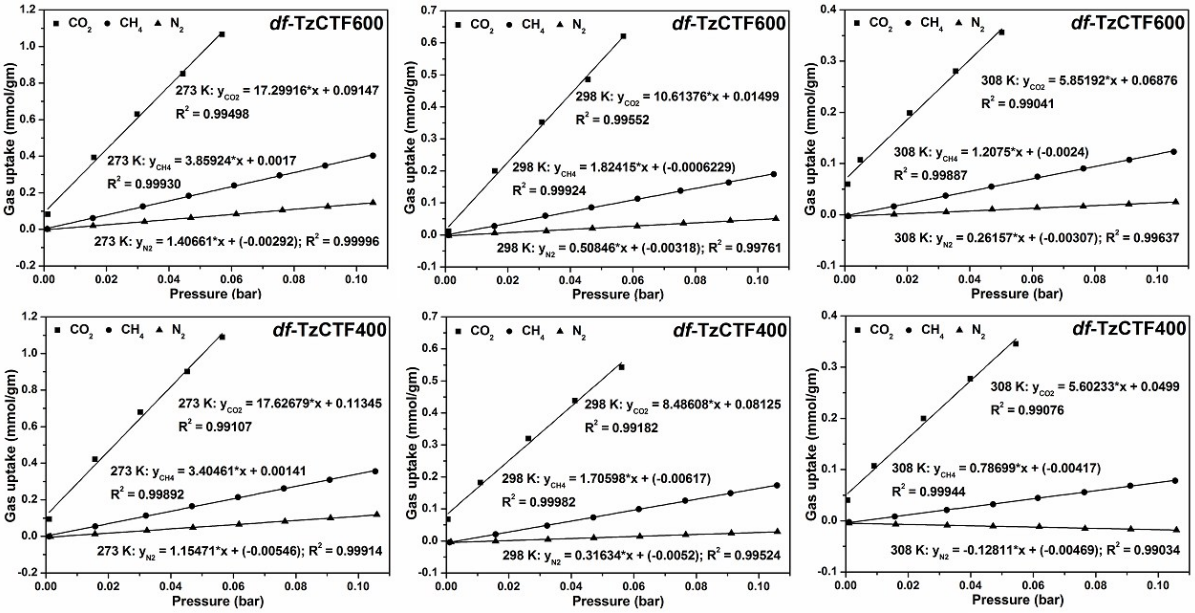

Figure S7: Henry plots of all TzCTF materials as derived from CO_2, N_2, and CH_4 isotherms at T = 273, 298, and 308 K.

Section J. Henry selectivity:

Table S2. CO_2/N_2 and CO_2/CH_4 selectivity measured on the TzCTF materials at T = 273, 298, and 308 K

Temp.	Initial slope of TzCTF series materials											
	TzCTF400			**TzCTF600**			***df*-TzCTF400**			***df*-TzCTF600**		
	CO_2	CH_4	N_2	CO_2	CH_4	N_2	CO_2	CH_4	N_2	CO_2	CH_4	N_2
273K	11.323	1.542	0.558	10.008	1.706	0.624	17.626	3.404	1.154	17.299	3.859	1.406
298K	5.348	0.963	0.226	4.960	0.967	0.284	8.486	1.705	0.316	10.613	1.824	0.508
308K	3.719	0.662	0.085	3.652	0.705	0.171	5.602	0.786	(-ve)	5.852	1.207	0.261

Temp.	Henry selectivity of TzCTF series materials by initial slop method[a]							
	TzCTF400		TzCTF600		***df*-TzCTF400**		***df*-TzCTF600**	
	CO_2/CH_4	CO_2/N_2	CO_2/CH_4	CO_2/N_2	CO_2/CH_4	CO_2/N_2	CO_2/CH_4	CO_2/N_2
273K	7.342	20.276	5.865	16.036	5.177	15.265	4.482	12.298
298K	5.551	23.638	5.125	17.424	4.974	26.78	5.818	20.868
308K	5.614	43.519	5.181	21.343	7.118	ND	4.846	22.37

ND: not determined as the initial slope is negative, [a]The selectivity of all TzCTF materials was measured from the ratio of the initial slopes in the Henry region of the respective CO_2, N_2, and CH_4 adsorption isotherms at T = 273, 298, and 308 K. The slopes of adsorption isotherms are obtained for each material by linear curve fitting as displayed in Figure S7.

Section K. Fitting of pure component isotherms:

The experimentally measured excess loadings of CO_2, and N_2, obtained at three different temperatures, 273 K, 298 K, and 308 K, were first converted to absolute loadings before data fitting. The data for both adsorption and desorption cycles were included in the data fitting. The procedure for converting to absolute loadings is the same as described in the Supporting Information accompanying the paper of Wu et al.[S7] For the purpose of converting to absolute loadings, the pore volumes used are specified in Table S3.

The isotherm data for CO_2 were fitted with the dual-site Langmuir model

$$q = q_{A,sat}\frac{b_A p}{1+b_A p} + q_{B,sat}\frac{b_A p}{1+b_B p} \quad (1)$$

The Langmuir fit parameters for adsorption of CO_2 are provided in Table S4 for *df*-TzCTF600, *df*-TzCTF400, TzCTF600, and TzCTF400. The simpler Langmuir model was adequate for fitting the isotherm data for N_2; Table S5 provides the Langmuir parameters for N_2 for *df*-TzCTF600, *df*-TzCTF400, TzCTF600, and TzCTF400. The isotherm fits are excellent for all four materials at all temperatures. This is demonstrated in the comparisons of experimental data and the isotherm fits for *df*-TzCTF600, *df*-TzCTF400, TzCTF600, and TzCTF400 in Figure S8.

Section L. Isosteric heat of adsorption:

The isosteric heat of adsorption, Q_{st}, defined as

$$Q_{st} = RT^2\left(\frac{\partial \ln p}{\partial T}\right)_q \quad (2)$$

were determined using the pure component isotherm fits using the Clausius-Clapeyron equation. Figure S9 presents a comparison of the isosteric heats of adsorption of CO_2 in *df*-TzCTF600, *df*-TzCTF400, TzCTF600, and TzCTF400 as a function of the CO_2 loading. The heats of adsorption of all four materials are close to one another.

Section M. IAST calculations of adsorption selectivities and uptake capacities:

The selectivity of preferential adsorption of component 1 over component 2 in a mixture containing 1 and 2, perhaps in the presence of other components too, can be formally defined as

$$S_{ads} = \frac{q_1/q_2}{p_1/p_2} \quad (3)$$

In equation (3), q_1 and q_2 are the *absolute* component loadings of the adsorbed phase in the mixture. These component loadings are also termed the uptake capacities. In all the calculations to be presented below, the calculations of q_1 and q_2 are based on the use of the Ideal Adsorbed Solution Theory (IAST) of Myers and Prausnitz.[S8]

For 15/85 mixtures, the IAST calculations of CO_2 and N_2 uptakes at 298 K in *df*-TzCTF600, *df*-TzCTF400, TzCTF600, and TzCTF400 are compared in Figure S10. We note that the uptake of both guest molecules is highest in *df*-TzCTF600 mainly because of its higher pore volume. The lowest CO_2 uptakes are for TzCTF400 and TzCTF600.

Figure S11 presents the values of the CO_2/N_2 adsorption selectivity for 15/85 flue gas mixture at 298 K using equation (3). We note that the CO_2/N_2 adsorption selectivity is highest for *df*-TzCTF400 and lowest for TzCTF600.

Section N. Transient breakthrough simulations in fixed bed adsorbers:

The separation of CO_2/N_2 mixtures is commonly carried out in fixed bed adsorbers in which the separation performance is dictated by a combination of three separate factors: (a) adsorption selectivity, and (b) uptake capacity. For a proper comparison of the performance of *df*-TzCTF600, *df*-TzCTF400, TzCTF600, and TzCTF400, we carried out transient breakthrough simulations that are representative of industrial fixed bed operations. The simulation methodology is as described in earlier publications.[94-96] For all the breakthrough calculations reported in this work, we assume negligible diffusion resistances for all materials

In order to evaluate the different adsorbents for use in a PSA unit, breakthrough calculations were performed using fixed beds of identical dimensions. The bulk densities of the packed materials are as specified in Table S3. For the breakthrough simulations, the following parameter values were used: length of packed bed, L = 0.3 m; voidage of packed bed, L = 0.4; superficial gas velocity at inlet, u = 0.04 m/s. The characteristic contact time between the adsorbent and the surrounding gas phase is $L\varepsilon/u$. It is common to use the dimensionless time, $\tau = tu/L\varepsilon$, obtained by dividing the actual time, t, by the characteristic time, $L\varepsilon/u$ when plotting simulated breakthrough curves. The operating temperature is 298 K and the total pressure is 1 bar. The partial pressures of CO_2 and N_2 at the feed gas inlet are 15 kPa, and 85 kPa, respectively.

The breakthrough calculations for *df*-TzCTF600, *df*-TzCTF400, TzCTF600, and TzCTF400 are compared in Figure 10 (main text). The *y*-axis in the plot is the concentration of the component in the outlet gas stream, normalized with respect the inlet composition.

A longer breakthrough time for CO_2 indicates better separation performance because more of CO_2 can be adsorbed in the bed before the need for regeneration. The best separations are achieved with *df*-TzCTF600. The reason for its good separation is mainly attributable to its high CO_2 uptake capacity (as noted in Figure S3), in combination with reasonably high CO_2/N_2 adsorption selectivity (see Figure S4). The poorest separation is achieved with TzCTF600, and the reason for its poor performance is due to the low CO_2 uptake capacity (see Figure S3), in combination with low CO_2/N_2 adsorption selectivity (see Figure S4).

Section O. Notation used in breakthrough simulation:

b Langmuir constant for species i at adsorption, Pa^{-1}

c_i molar concentration of species i in gas mixture, mol m^{-3}

c_{i0} molar concentration of species i in gas mixture at inlet to adsorber, mol m^{-3}

L length of packed bed adsorber, m

p_i partial pressure of species i in mixture, Pa

p_t total system pressure, Pa

q_i component molar loading of species i, mol kg^{-1}

t time, s

T absolute temperature, K

u superficial gas velocity in packed bed, m s^{-1}

Greek letters

ε voidage of packed bed, dimensionless

ρ framework density, kg m^{-3}

τ time, dimensionless

Subscripts

i referring to component i

t referring to total mixture

Section P. Supporting tables:

Table S3. Salient properties of *df*-TzCTF600, *df*-TzCTF400, TzCTF600, and TzCTF400.

Material	Bulk density (g cm^{-3})	Pore volume (cm^3 g^{-1})
df-TzCTF600	0.337	1.124
df-TzCTF400	0.292	0.7057
TzCTF600	0.348	1.02
TzCTF400	0.544	0.6949

Table S4. Dual-site Langmuir parameters for adsorption of CO_2 in *df*-TzCTF600, *df*-TzCTF400, TzCTF600, and TzCTF400. The experimentally measured excess loadings were first converted to absolute loadings before data fitting.

Material	Temperature T/ K	Site A		Site B	
		$q_{A,sat}$ mol kg^{-1}	b_A Pa^{-1}	$q_{B,sat}$ mol kg^{-1}	B_B Pa^{-1}
df-TzCTF600	273 K	0.9	2.63×10^{-4}	15.5	6.22×10^{-6}
df-TzCTF600	298 K	0.9	1.12×10^{-4}	15.5	3.16×10^{-6}

df-TzCTF600	308 K	0.9	5.43×10^{-5}	15.5	1.74×10^{-6}
df-TzCTF400	273 K	1.4	1.91×10^{-4}	9.8	7.33×10^{-6}
df-TzCTF400	298 K	1.4	6.94×10^{-5}	9.8	2.75×10^{-6}
df-TzCTF400	308 K	1.4	3.9×10^{-5}	9.8	1.43×10^{-6}
TzCTF600	273 K	0.7	1.71×10^{-4}	11.4	4.91×10^{-6}
TzCTF600	298 K	0.7	5.24×10^{-5}	11.4	2.1×10^{-6}
TzCTF600	308 K	0.7	3.44×10^{-5}	11.4	1.55×10^{-6}
TzCTF400	273 K	1.05	1.3×10^{-4}	8.1	6.74×10^{-6}
TzCTF400	298 K	1.05	3.44×10^{-5}	8.1	2.71×10^{-6}
TzCTF400	308 K	1.05	2.15×10^{-5}	8.1	1.96×10^{-6}

Table S5. Single-site Langmuir parameters for N_2 in *df*-TzCTF600, *df*-TzCTF400, TzCTF600, and TzCTF400.

Material	Temperature *T*/ K	$q_{A,sat}$ (mol kg^{-1})	b_A (Pa^{-1})
df-TzCTF600	273 K	15	9.48×10^{-7}
df-TzCTF600	298 K	15	3.32×10^{-7}
df-TzCTF600	308 K	15	1.49×10^{-7}
df-TzCTF400	273 K	7	1.9×10^{-6}
df-TzCTF400	298 K	7	4.42×10^{-7}
TzCTF600	273 K	13	5.34×10^{-7}
TzCTF600	298 K	13	2.25×10^{-7}
TzCTF600	308 K	13	1.65×10^{-7}
TzCTF400	273 K	15	3.8×10^{-7}
TzCTF400	298 K	15	1.5×10^{-7}
TzCTF400	308 K	15	7.0×10^{-8}

Table S6. Comparison of surface area, CH_4 uptake (> 2 wt% at 273 K) and Q_{st} of other high-performing POP and CTF based adsorbents at 1 bar.

POP & CTF-based adsorbents	S_{BET} (m^2 g^{-1})	CH_4 Uptake [wt%]		Q_{st} [KJ mol^{-1}]	Ref.
	77K	273 K	298 K		
TPC-1	1940	6.2	-	-	**60**
df-TzCTF600	1720	4.38	2.18	23.5	Current work
df-TzCTF400	906	3.57	2.06	24.2	Current work
TzCTF600	1582	2.17	1.24	21.2	Current work
TzCTF400	874	1.68	1.15	21.3	Current work
PPOP-1	720	4.01	-	-	**S15**
PPOP-2	920	4.29	-	-	
PPOP-3	880	3.24	-	-	
BDT-3	1010	2.9	-	-	**S16**

BILP-6-NH_2	1185	2.8	-	-	**S17**
TPMTP	890	2.7	-	-	**S18**
PCTF-4	1404	2.7	-	-	**24**
BILP-6	1261	2.7	1.90	13.2	**S19**
BILP-3	1306	2.4	1.70	16.6	
ALP-1	1235	2.6	1.50	20.8	**S20**
Cz-POF-3	1927	2.54	1.71[a]	20.2	**S21**
Cz-POF-1	2065	2.29	1.56[a]	19	
BILP-4	1135	2.53	1.80	13.0	**S22**
PPF-1	1740	2.43	-	15.1	**96**
PPF-2	1470	2.31	-	15.9	
BILP-12	1497	2.4	1.50	18.6	**S23**
TNP-4	1348	2.38	1.42	20	**S24**
MM2	1360	2.34	1.51[b]	-	**51**
MM1	1800	2.06	1.34[b]	-	
CTF-TPC	1668	2.14	-	-	**S14**
PAF-60	1094	2.0	1.50	24.1	**S25**
JUC-Z8	4743	2.0	-	-	**S26**

[a]measured at 290 K. [b]measured at 293 K

Table S7. Comparison of structural parameters, CO_2 (> 4 mmol g^{-1} at 273 K) and H_2 uptakes, and CO_2/N_2 selectivity of TzCTFs materials with other most representative related CTF-based adsorbents

CTF-based adsorbents	S_{BET} (m^2 g^{-1})	CO_2 Uptake [mmol g^{-1}]			Q_{st} [KJ mol^{-1}]	Selectivity$^{298\ K}$ (CO_2/N_2)		H_2 Uptake [wt%]	Ref.
	77 K	273 K	298 K	308 K		Henry	IAST	77 K	
df-TzCTF600	1720	6.79	4.60	3.00	34	17	30	2.50	Current work
df-TzCTF400	906	5.51	3.32	2.32	35	22	40	2.16	Current work
TzCTF600	1582	4.40	2.51	2.03	28	16	21	2.06	Current work
TzCTF400	874	4.21	2.55	1.90	32	21	26	1.75	Current work
HAT-CTF 450/600	1090	6.3	-	-	27.1	-	-	-	**23**
HAT-CTF-600	899	5.1	-	-	-	-	-	-	
HAT-CTF-450	756	4.4	-	-	-	-	-	-	
F-DCBP-CTF-1	2437	5.98	3.82	-	33.1	31	-	1.77	**57**
F-DCBP-CTF-2	2036	5.23	3.16	-	-	22	-	-	
CTF-py	1239	5.08	3.79	-	35.1	45	-	1.63	**95**
CTF-ph	1991	4.54	3.05	-	33.2	20	-	1.87	
bipy-CTF500	1548	5.34	3.07	1.77[a]	34.2	61	42	1.63	**56**
bipy-CTF600	2479	5.58	2.95	1.84[a]	34.4	37	24	2.10	
lut-CTF350	635	4.06	2.41	1.59[a]	37.4	76	66	1.22	

lut-CTF400	968	4.55	2.72	1.80[a]	37.5	63	53	1.36	
lut-CTF500	1680	5.04	2.58	1.71[a]	38.2	27	27	1.60	
lut-CTF600	2815	4.99	2.52	1.66[a]	33.3	26	23	2.00	
FCTF-1-600	1535	5.53	3.41	-	-	-	19	-	**55**
FCTF-1	662	4.67	3.21	-	35	-	31	-	
*p*CTF-1	2034	4.97	-	-	25.9	-	-	1.75	**S9**
TPC-1	1940	4.90	-	-	39	38[b]	-	2.00	**60**
MM2	1360	4.77	-	-	32	23[b]	44[b]	1.74	**51**
PCTF-4	1404	4.65	2.86	-	~31	56[b]	-	1.30	**24**
fl-CTF-350	1235	4.28	2.29	1.59[a]	32.7	27	23	-	**21**
fl-CTF-400	2862	4.13	1.97	1.31[a]	30.7	15	16	1.95	
CTF-0	2011	4.22	-	-	-	-	-	-	**22**
P6M	947	4.17	-	-	-	-	14.2[b]		**S10**
PCTP-1	1200	4.91	3.24	2.56[c]	44.5	46.1	-	-	**S11**
CTF-BI-4	1025	4.85	-	2.72[c]	34.3–31.7	44.0[b]	-	-	**S12**
CTF-BI-5	836	4.49	-	2.68[c]		35.6[b]	-	-	
CTF-BI-9	885	4.29	-	2.36[c]		67.4[b]	-	-	
CTF-BI-10	1099	4.45	-	2.58[c]		31.3[b]	-	-	
CTF-BI-11	1549	4.93	-	2.63[c]		34.3[b]	-	-	
MCTP-1	1452	4.64	2.69	1.82	40.0	15.4	-	-	**S13**
CTF-TPC	1668	4.25			32	20.0[b]	30.0[b]	1.75	**S14**

[a]measured at 313 K, [b]measured at 273 K. [c]measured at 303 K

Section Q. Supporting figures:

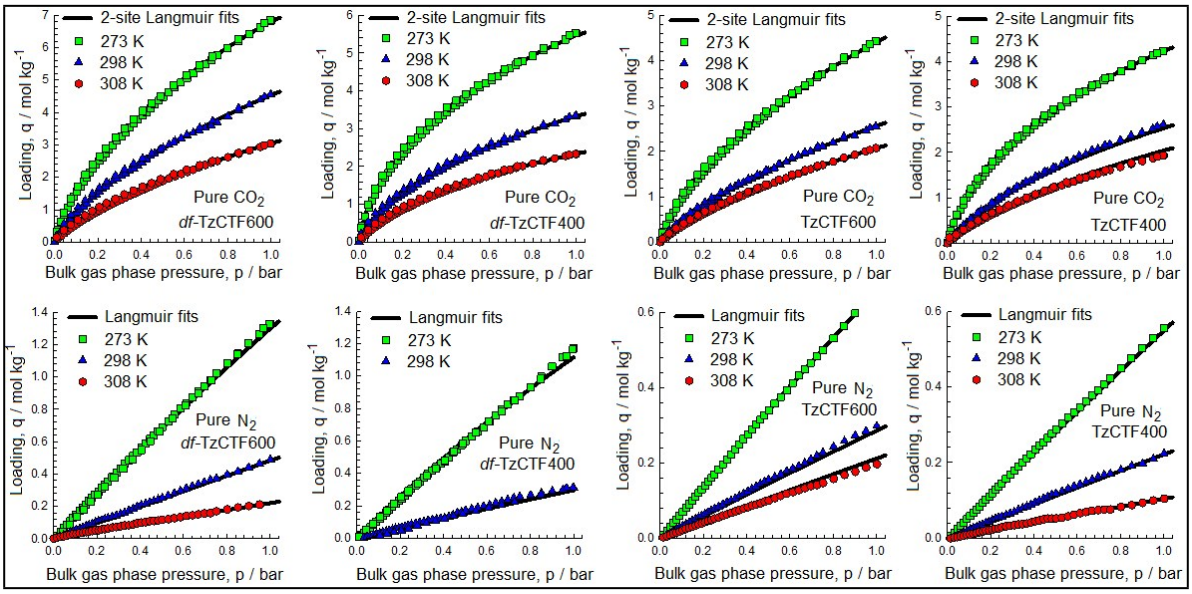

Figure S8. Comparison of the pure component isotherm data in *df*-TzCTF600, *df*-TzCTF400, TzCTF600, and TzCTF400 with the fitted isotherms (shown by continuous solid lines) at various temperatures.

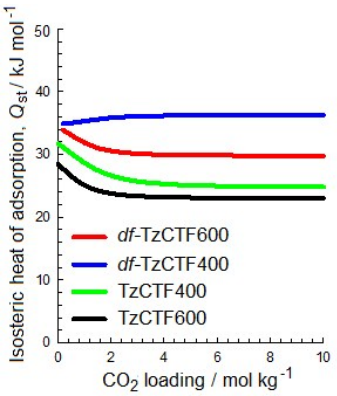

Figure S9. Comparisons of the isosteric heats of adsorption of CO_2 in *df*-TzCTF600, *df*-TzCTF400, TzCTF600, and TzCTF400 as a function of the CO_2 loading.

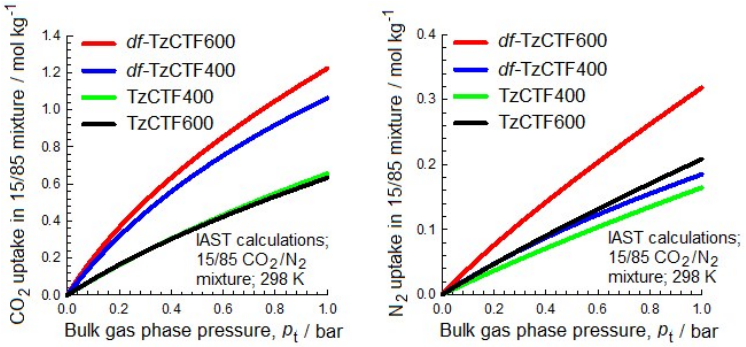

Figure S10. Calculations using Ideal Adsorbed Solution Theory (IAST) of Myers and Prausnitz[S8] for uptakes of CO_2 and N_2, expressed as moles per kg of adsorbent, in equilibrium with binary CO_2/N_2 gas mixture maintained at isothermal conditions at 298 K. In these calculations the partial pressures of CO_2 and N_2 are taken to be p_1/p_2 = 15/85.

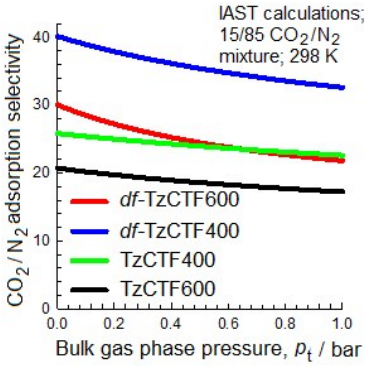

Figure S11. Calculations using Ideal Adsorbed Solution Theory (IAST) of Myers and Prausnitz[S8] for CO_2/N_2 adsorption selectivity for a binary CO_2/N_2 gas mixture maintained at isothermal conditions at 298 K. In these calculations the partial pressures of CO_2 and N_2 are taken to be p_1/p_2 = 15/85.

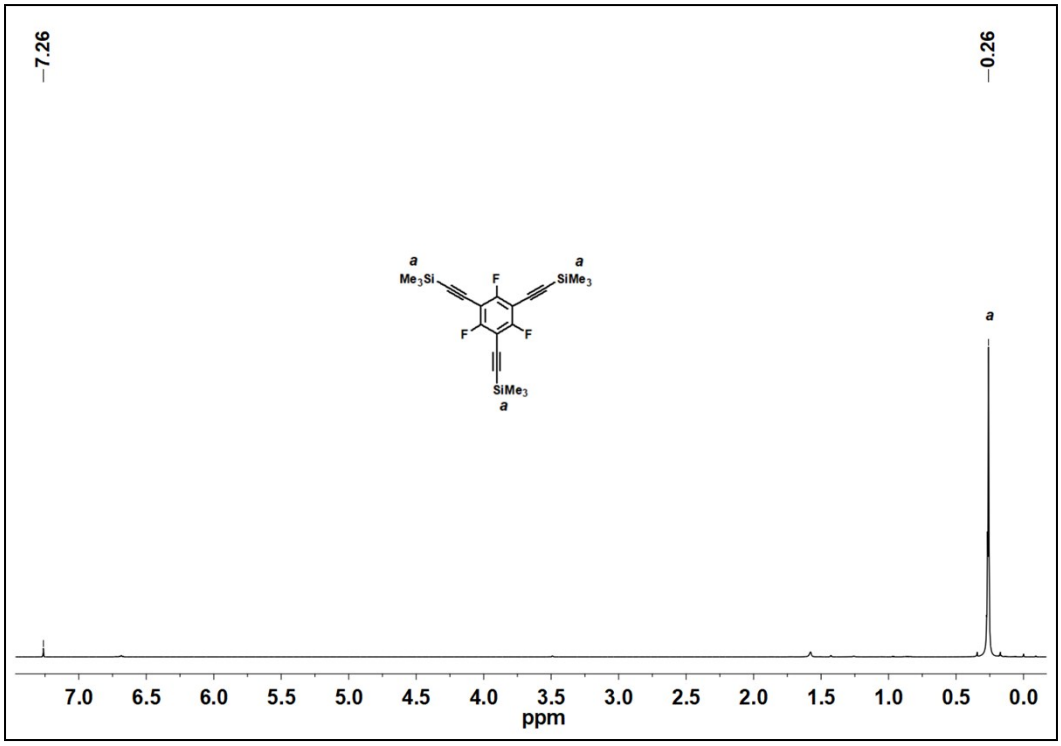

Figure S12: ^{1}H NMR of 1,3,5-trifluoro-2,4,6-tris[(trimethylsilyl)ethynyl)]benzene

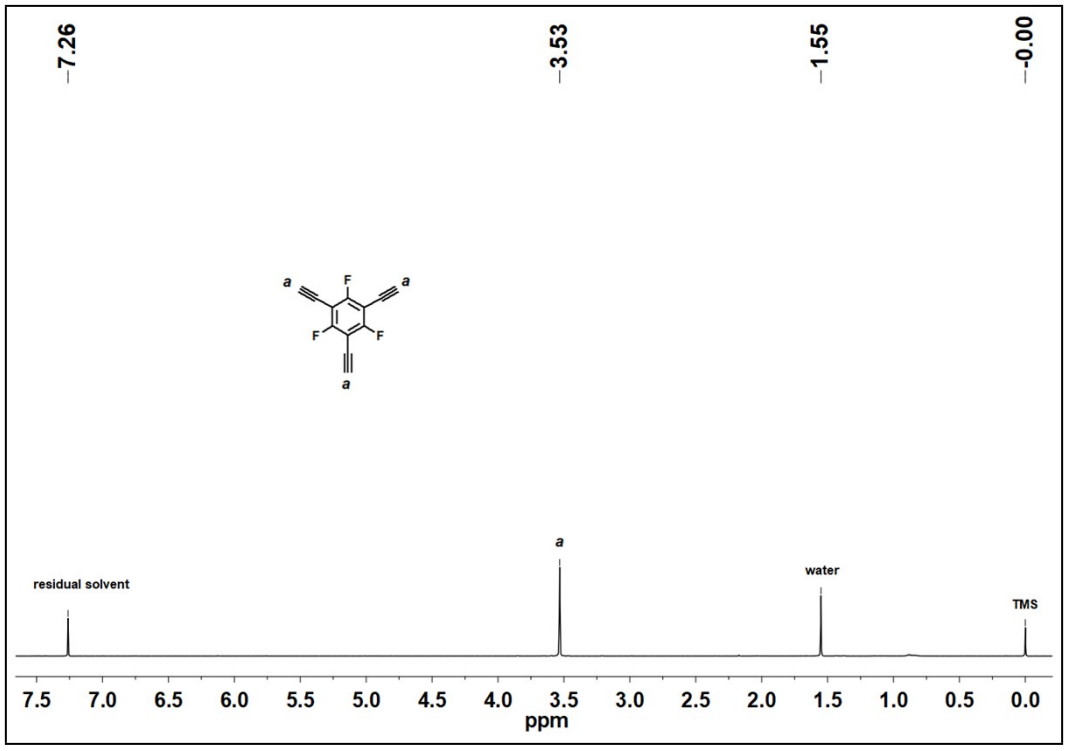

Figure S13: ^{1}H NMR of 1,3,5-triethynyl-2,4,6-trifluorobenzene

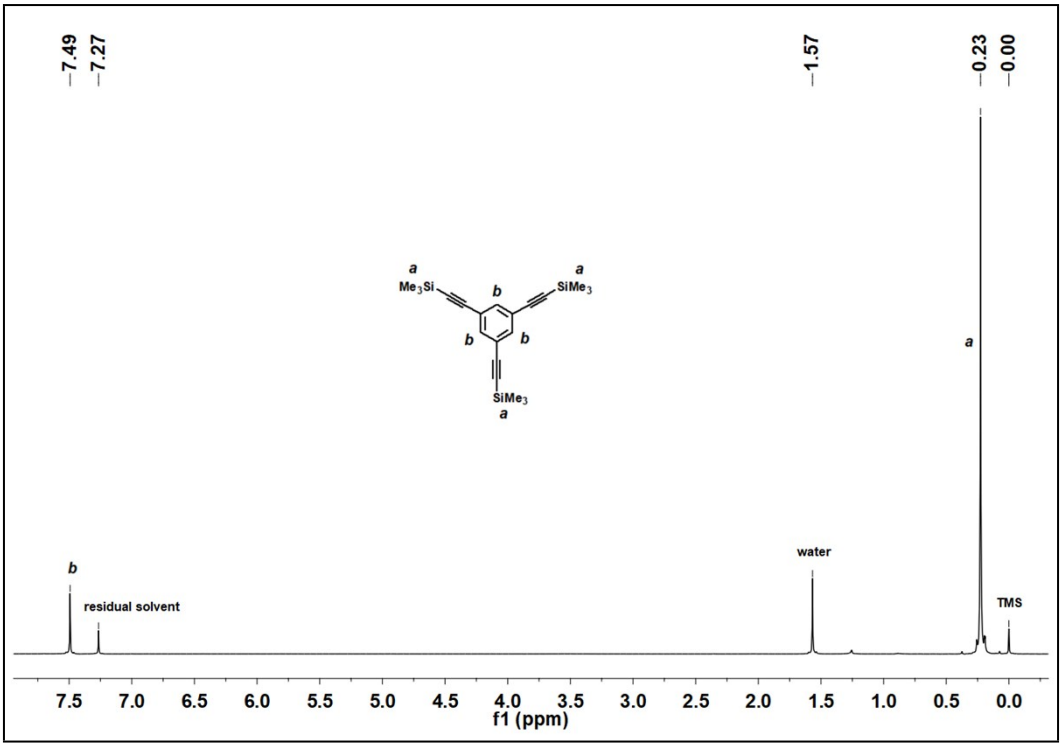

Figure S14: ^{1}H NMR of 1,3,5-tris[2-(trimethylsilyl)ethynyl]benzene

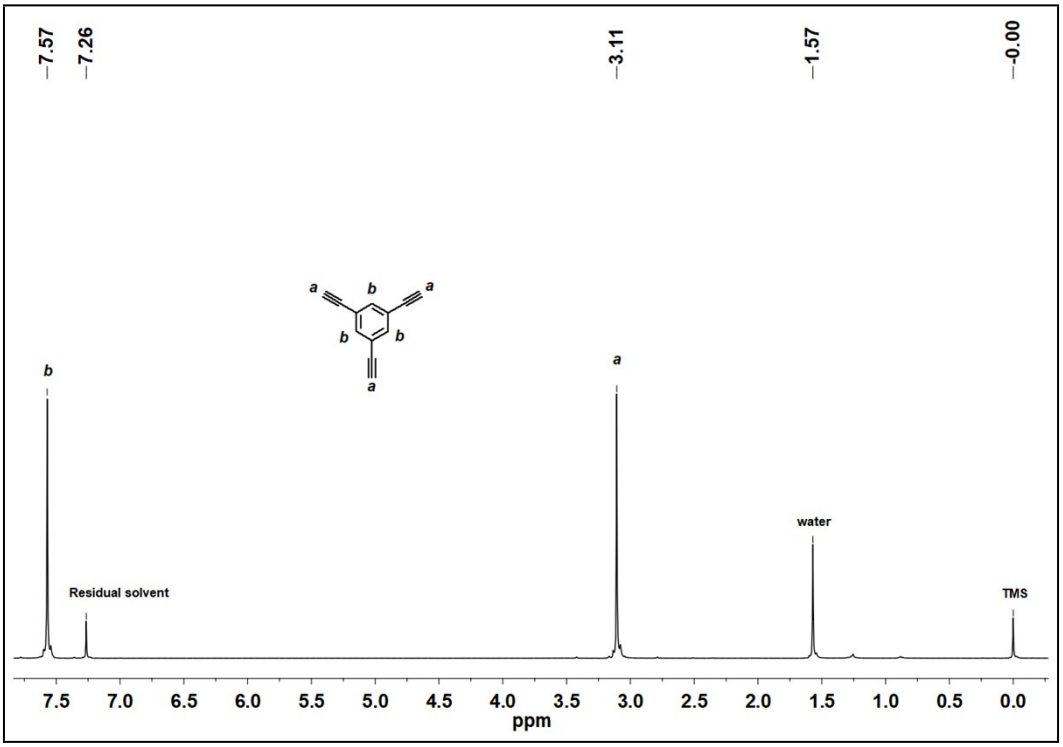

Figure S15: ^{1}H NMR of 1,3,5-triethynylbenzene

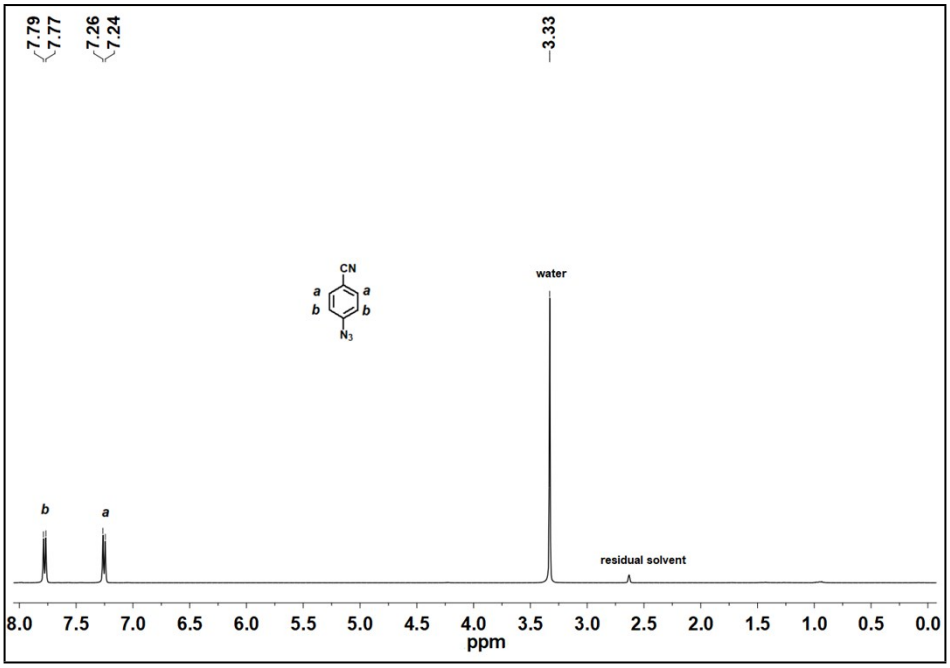

Figure S16: ^{1}H NMR of 4-azidobenzonitrile.

As per the reviewer comment, soluble model compound (**MC-1**) has been synthesized to justify further the successful formation of current building blocks Tz-HCN and Tz-FCN via "*click reaction*".

Section R. Structure, synthesis, and charactrization of Model Compounds:

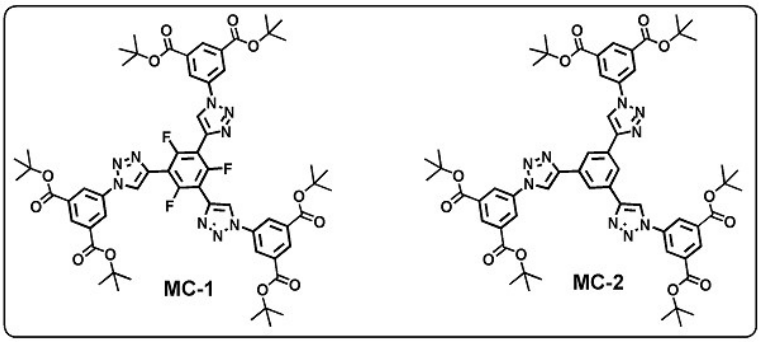

Chart S1: Chemical structure of model compound, **MC-1** and **MC-2**. The synthesis of **MC-2** is already reported by X.-J. Wang et al. in *Scientific Report*, 2013, **3**, 1149.[S27]

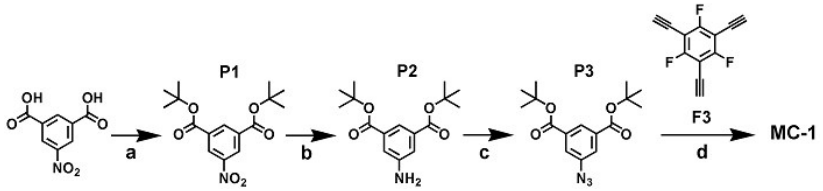

Scheme S2: Synthetic route of **MC-1** (a): DMAP, DCC, tert-Butanol; (b): Pd/C, ammonium formate, MeOH; (c): HCl, sodium nitrite, NaN_3, Methanol, 0^{o}C; (d): Sodium ascorbate, $CuSO_4.5H_2O$, Water, Tetrahydrofuran, 40^{o}C, 3 days.

Synthesis of Di-*tert*-butyl 5-nitroisophthalate (P1):[S28] It was synthesized from 5-nitroisophthalic acid using literature method and purified by column chromatography (100% $CHCl_3$) to get 6.3 g of white solid (65%). ^1H NMR (400 MHz; $CDCl_3$): 1.64 (s, 18H), 8.92 (d, 2H), 8.87 (t, 1H)

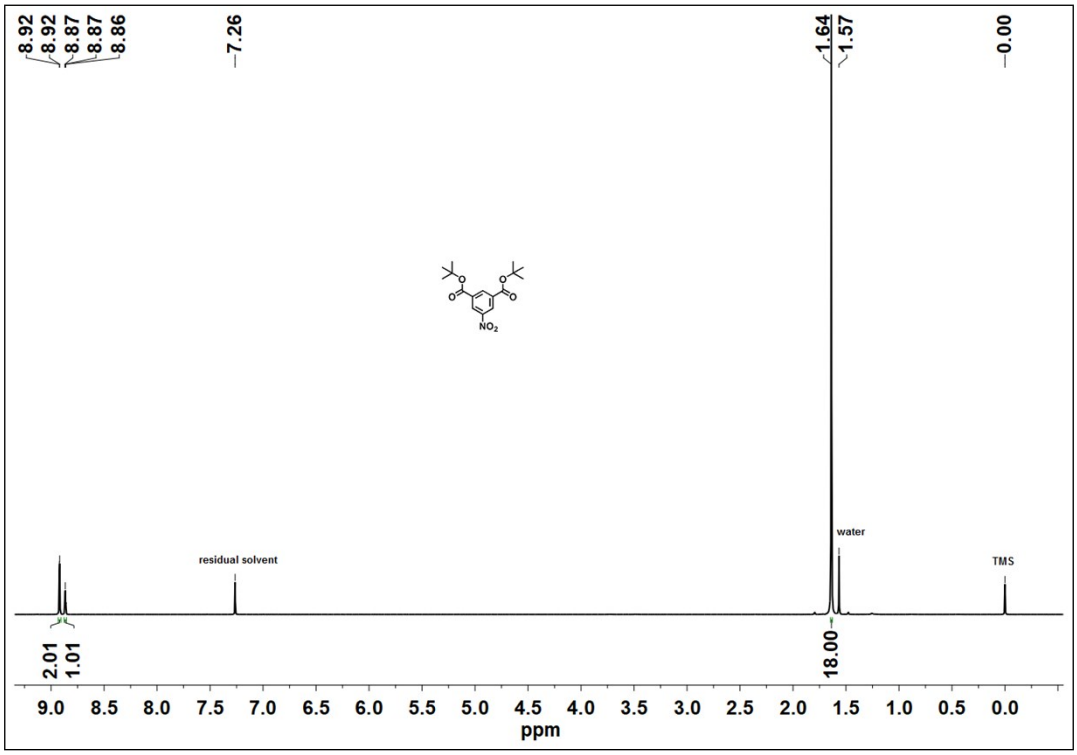

Figure S17: ^1H NMR of di-*tert*-butyl 5-nitroisophthalate, **P1**

Synthesis of Di-*tert*-butyl 5-aminoisophthalate (P2):[S29] It was synthesized from di-*tert*-butyl 5-nitroisophthalate using literature method with quantitative yield and the as-synthesized compound is used in next step without any further characterization.

Synthesis of Di-*tert*-butyl 5-azidoisophthalate (P3):[S27] A 250 ml round bottom flask equipped with stir bar was charged with di-*tert*-butyl 5-aminoisophthalate (4.7 g, 16.02 mmol), MeOH (175 ml) and HCl (0.5 M, 175 ml). The reaction mixture was cooled down to 0-5^{0}C and stirred for 1 hour. Ice-cold solution of sodium nitrite (3.31 g, 48.06 mmol) was added dropwise into the reaction mixture and stirring was continued for 1 hour. Then the reaction mixture was slowly poured into a solution of NaN_3 (3.16 g, 48.5 mmol) at 0^{o}C. The combined reaction mixture was then stirred for additional 1.0 hour. The reaction mixture was then extracted by dichloromethane (3 x 50 ml). The combined organic layer was washed with water and dried over anhydrous $MgSO_4$. The organic layer was evaporated to dryness under reduced pressure to obtain crude product which was purified by silica gel column

chromatography (hexane:dichloromethane 5:5) yielding **P1** (3.84 g, 75 %) as white solid. ^{1}H NMR (400 MHz; $CDCl_3$): 1.61 (s, 18H), 7.78 (d, 2H), 8.32 (t, 3H)

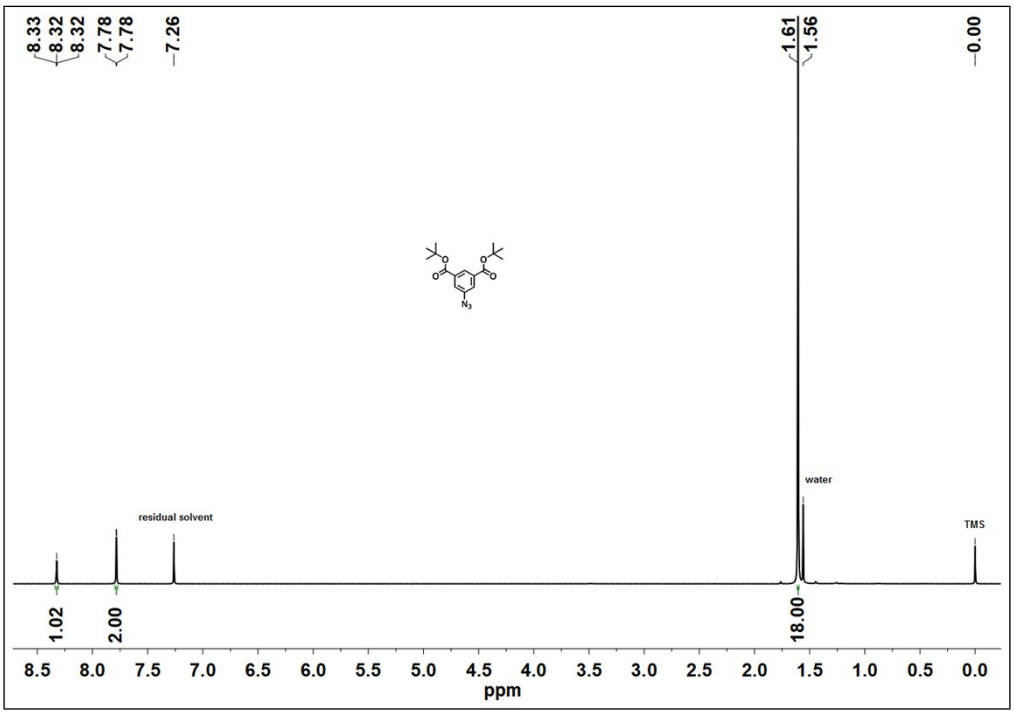

Figure S18: ^{1}H NMR spectra of precursor, **P3**

Synthesis of model compound (MC-1): A 250 ml round bottom flask equipped with stir bar was charged with 1,3,5-triethynyl-2,4,6-trifluorobenzene, **F3** (210 mg, 1.02 mmol), di-*tert*-butyl-5-azidoisophthalate, **P3** (1.11 g, 3.49 mmol), THF (100 ml), and water (40 ml). The resulting solution was purged with argon over 30 min at room temperature followed by addition of $CuSO_4.5H_2O$ (80 mg, 0.32 mmol) and sodium ascorbate (127 mg, 0.64 mmol). The reaction mixture was heated to 40^{o}C and kept stirring for 3 days under inert atmosphere. After completion of the reaction THF was evaporated and organic part was extracted by DCM (3 x 25 ml) and washed with water followed by drying over anhydrous $MgSO_4$. Organic layer was evaporated to dryness and the crude product was purified via column chromatography (silica gel, ethyl acetate:dichloromethane 0.2:9.8) to obtain cream colored solid compound (609 mg, 51%). ^{1}H NMR (400 MHz; $CDCl_3$): 1.66 (s, 54H), 8.58 (s, 3H), 8.59-8.60 (d, 6H), 8.70 (t, 3H)

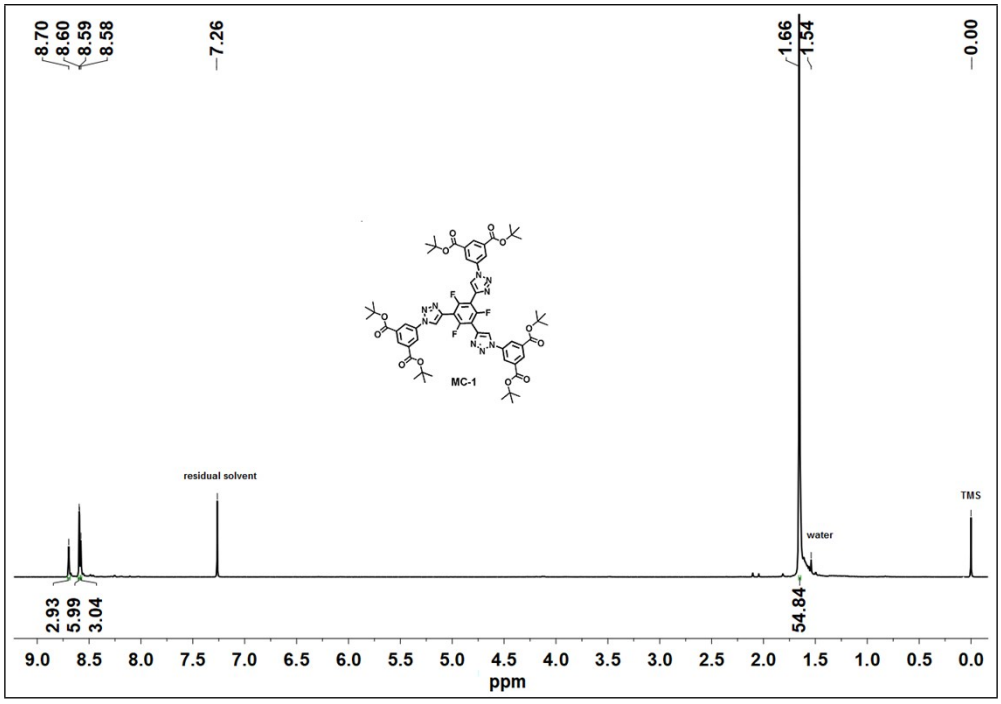

Figure S19: ^{1}H NMR spectra of **MC-1**

As per the reviewer suggestion, TzCTFs synthesis were made at 700^{o}C using both fluorinated (Tz-FCN) and non-fluorinated (Tz-HCN) building block and evaluated their textural and gas adsorption properties to further address the synthesis temperature effect on gas uptake properties in TzCTFs series materials.

Section S. Gas uptake experiments and textural properties:

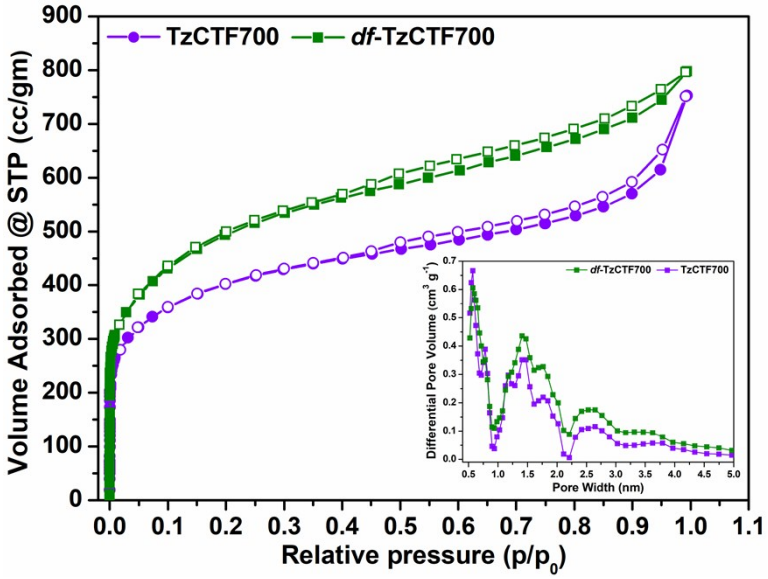

Figure S20: Nitrogen adsorption-desorption isotherms measured at 77 K (the solid and open symbols represent adsorption and desorption, respectively); the inset display the pore size distribution calculated by the NL-DFT method.

Table S8: Porosity data derived from N_2 isotherm (77 K, 1 bar) of TzCTFs materials synthesized at 700°C

Material	S_{BET}[a] ($m^2\ g^{-1}$)	S_{Lang}[b] ($m^2\ g^{-1}$)	$V_{0.1}$[c] ($cm^3\ g^{-1}$)	V_{tot}[d] ($cm^3\ g^{-1}$)	$V_{0.1}/V_{tot}$	V_{micro}[e] (CO_2) ($cm^3\ g^{-1}$)
***df*-TzCTF700**	1628	1921	0.66	1.24	0.53	0.040
TzCTF700	1307	1582	0.55	1.16	0.47	0.033

[a]Calculated BET surface area over the pressure range 0.05-0.3 P/P_0. [b]Langmuir surface area calculated by applying Langmuir equation on nitrogen adsorption isotherm over the pressure range 0-0.15 P/P_0. (c) Micropore volume calculated at P/P_o = 0.1 for pores with diameter smaller than 1.6 nm. (d) Total pore volume calculated at P/P_o = 0.99. (e) Total pore volume for pores with diameters smaller than 0.9 nm at P/P_o = 0.1 calculated from CO_2 adsorption isotherm at 273 K (NL-DFT model).

Table S9: Gas uptake properties for the presented TzCTF materials synthesized at 700°C

Material	CO_2 Uptake[a]			CH_4 Uptake[c]		H_2 Uptake[c]
	273 K	298 K	Q_{st}[b]	273 K	298 K	77 K
***df*-TzCTF700**	4.68 (1.16)	3.04	25	1.96	1.26	2.12
TzCTF700	4.06 (0.95)	2.55	31	1.46	0.98	1.67

[a]Gas uptake in mmol g^{-1} at 1 bar and values in parenthesis in mmol g^{-1} at 0.15 bar , [b]Isosteric heat of adsorption at zero coverage in kJ mol^{-1}, [c]Gas uptake in wt% at 1 bar.

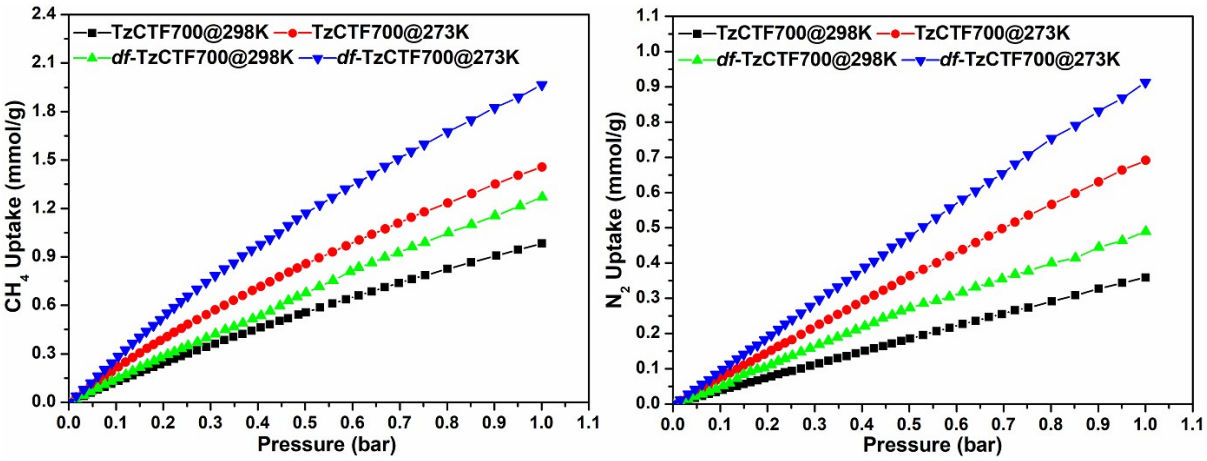

Figure S21: (a) CH_4 adsorption (left) and (b) N_2 adsorption (right) of *df*-TzCTF700 and TzCTF700 material measured at 273 K and 298 K under 1 bar

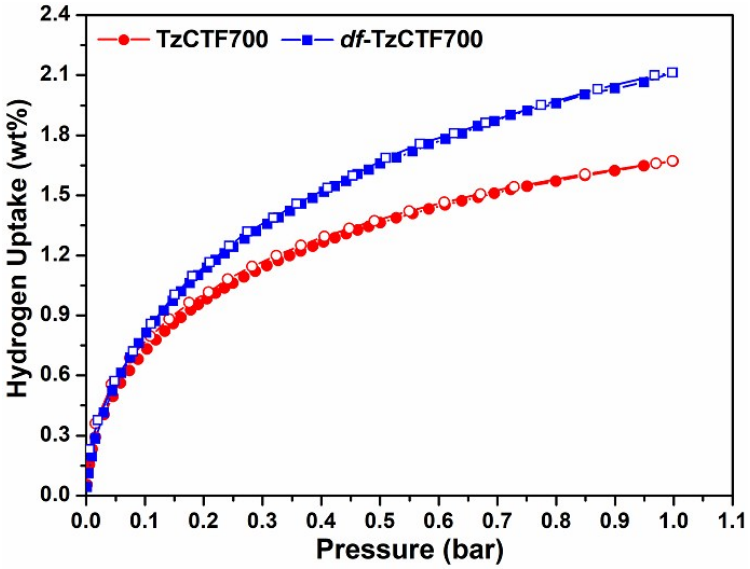

Figure S22: (a) H_2 adsorption-desorption isotherm of *df*-TzCTF700 and TzCTF700 material measured at 77 K under 1 bar

Table S10: Comparison of textural and gas adsorption properties of our highest performing *df*-TzCTF600 material with other high-performing related CTF-based materials

CTF-based adsorbents	S_{BET} ($m^2\ g^{-1}$)	S_{micro} ($m^2\ g^{-1}$)	V_{micro} [$cm^3\ g^{-1}$]	CO_2 Uptake [mmol g^{-1}]		CH_4 Uptake [wt%]	H_2 Uptake [wt%]	Ref.
				273 K	298 K	273 K	77 K	
df-TzCTF600	1720	1505	0.75	6.79	4.60	4.38	2.50	Current work
HAT-CTF 450/600	1090	ND	ND	6.3	-	-	-	23
HAT-CTF-600	899	ND	ND	5.1	-	-	-	
F-DCBP-CTF-1	2437	ND	0.51	5.98	3.82	-	1.77	57
F-DCBP-CTF-2	2036	ND	0.34	5.23	3.16	-	-	
CTF-py	1239	ND	0.45	5.08	3.79	-	1.63	95
bipy-CTF500	1548	ND	ND	5.34	3.07	-	1.63	56
lut-CTF500	1680	ND	ND	5.04	2.58	-	1.60	
FCTF-1-600	1535	752	ND	5.53	3.41	ND	ND	55

ND: not determined

Section T. Supporting References:

References:

S1:	H. H. Wenk and W. Sander, *Eur. J. Org. Chem.,* 2002, **23**, 3927-3935.
S2:	Y. Tobe, N. Nakagawa, J. Kishi, M. Sonoda, K. Naemura, T. Wakabayashi, T. Shida, and Y. Achiba, *Tetrahedron,* 2001, **57**, 3629-3636.
S3:	O. K. Farha, A. Ö. Yazaydın, I. Eryazici, C. D. Malliakas, B. G. Hauser, M. G. Kanatzidis, S. T. Nguyen, R. Q. Snurr and J. T. Hupp, *Nature Chemistry,* 2010, **2**, 944-948.

S4:	Y. -L. Zhao, L. Liu, W. Zhang, C. -H. Sue, Q. Li, O. Š. Miljanić, O. M. Yaghi and J. F. Stoddart, *Chem. Eur. J.*, 2009, **15**, 13356-13380.
S5:	K. V. Kutonova, M. E. Trusova, P. S. Postnikov, V. D. Filimonov and J. Parello *Synthesis,* 2013, **45**, 2706-2710.
S6:	M. Matti Maricq and J. S. Waugh, *J. Chem. Phys.,* 1979, **70**, 3300-3316.
S7:	H. Wu, K. Yao, Y. Zhu, B. Li, Z. Shi, R. Krishna and J. Li, *J. Phys. Chem. C,* **2012**, *116*, 16609-16618.
S8:	A. L. Myers and J. M. Prausnitz, *A.I.Ch.E.J.* 1965, **11**, 121-130.
S9:	S. -Y. Yu, J. Mahmood, H. -J. Noh, J. -M. Seo, S. -M. Jung, S. -H. Shin, Y. -K. Im, I. -Y. Jeon and J. -B. Baek, *Angew. Chem. Int. Ed*., 2018, **57**, 8438-8442.
S10:	S. Ren , M. J. Bojdys , R. Dawson , A. Laybourn , Y. Z. Khimyak , D. J. Adams and A. I. Cooper, *Adv. Mater.,* 2012, **24**, 2357-2361.
S11:	P. Puthiaraj, S. -S. Kim and W. -S. Ahn, *Chem. Eng. J*., 2016, **283**, 184-192.
S12:	L. Tao, F. Niub, C. Wanga, J. Liuc, T. Wanga and Q. Wang, *J. Mater. Chem. A*, 2016, **4**, 11812-11820.
S13:	P. Puthiaraj, S. -M. Cho, Y.-R. Lee and W. -S. Ahn, *J. Mater. Chem. A*, 2015, **3**, 6792-6797.
S14:	S. Dey, A. Bhunia, D. Esquivel and C. Janiak, *J. Mater. Chem. A*, 2016, **4**, 6259-6263.
S15:	T.Wang, Y.-C. Zhao, L.-M. Zhang, Y. Cui, C.-S. Zhang and B. -H. Han, *Beilstein J. Org. Chem.,* 2017**, 13**, 2131-2137.
S16:	S. Bandyopadhyay, A. G. Anil, A. James and A. Patra, *ACS Appl. Mater. Interfaces*, 2016, **8**, 27669-27678.
S17:	T. Islamoglu, S. Behera, Z. Kahveci, T.-D. Tessema, P. Jena and H. M. El-Kaderi, *ACS Appl. Mater. Interfaces*, 2016, **8**, 14648-14655.
S18:	MD. W. Hussain, S. Bandyopadhyay and A. Patra, *Chem. Commun.,* 2017, **53**, 10576-10579.
S19:	M. G. Rabbani, T. E. Reich, R.M. Kassab, K. T. Jackson and H. M. El-Kaderi, *Chem. Commun.,* 2012, **48**, 1141-1143.
S20:	P. Arab, M. G. Rabbani, A. K. Sekizkardes, T. İslamoğlu and H. M. El-Kaderi, *Chem. Mater.*, 2014, **26**, 1385-1392.
S21:	X. Zhang, J. Lu and J. Zhang, *Chem. Mater.*, 2014, **26**, 4023-4029.
S22:	M. G. Rabbani and H. M. El-Kaderi, *Chem. Mater.*, 2012, **24**, 1511-1517.
S23:	A. K. Sekizkardes, T. Islamoğlu, Z. Kahveci and H. M. El-Kaderi, *J. Mater. Chem. A*, 2014, **2**, 12492-12500.
S24:	S. Mondal and N. Das, *J. Mater. Chem. A*, 2015, **3**, 23577-23586.
S25:	Y. Yuan, P.Cui, Y. Tian, X. Zou, Y. Zhou, F. Sunb and G. Zhu, *Chem. Sci*., 2016, **7**, 3751-3756.
S26:	C. Pei, T. Ben, Y. Li and S. Qiu, *Chem. Commun.,* 2014, **50**, 6134-6136.
S27	X. –J. Wang, P. –Z. Li, Y. Chen, Q. Zhang, H. Zhang, X. X. Chan, R. Ganguly, Y. Li, J. Jiang and Y. Zhao, *Scientific Report*, 2013, **3**, 1149
S28	J. M. Roberts, B. M. Fini, A. A. Sarjeant, O. K. Farha, J.T. Hupp and K. A. Scheidt, *J. Am. Chem. Soc.*, 2012, **134**, 3334.
S29	R. Luebke, Ł. J. Weseliński, Y. Belmabkhout, Z. Chen, Ł. Wojtas and M. Eddaoudi, *Cryst. Growth Des.*, 2014, **14**, 414.